www.sciencemag.org/content/350/6264/aac9462/suppl/DC1

Supplementary Materials for

Principles of connectivity among morphologically defined cell types in adult neocortex

Xiaolong Jiang,* Shan Shen, Cathryn R. Cadwell, Philipp Berens, Fabian Sinz, Alexander S. Ecker, Saumil Patel, Andreas S. Tolias*

*Corresponding author. E-mail: astolias@bcm.edu (A.S.T).; xiaolonj@bcm.edu (X.J.)

Published 27 November 2015, *Science* **350**, aac9462 (2015)
DOI: 10.1126/science.aac9462

This PDF file includes:

Materials and Methods
Supplementary Text
Figs. S1 to S14
Tables S1 to S10
References

Materials and Methods

Animal preparation

Procedures for mouse maintenance and mouse surgeries were performed according to protocols approved by the Institutional Animal Care and Use Committee (IACUC) of Baylor College of Medicine. Adult male and female wild type (n=45) and Viaat-Cre/Ai9 mice (n=85) were used in most of experiments, and SOM-Cre/Ai9 mice (n = 30), VIP-Cre/Ai9 mice (n =5), or PV-Cre/Ai9 mice (n = 18) were also used (≥~2 month PND). *Viaat* encodes a transporter required for loading GABA, as well as glycine, into synaptic vesicle (*40,41*). Crossing Viaat-Cre mice with ai9 reporter mice globally labels GABAergic interneurons with the fluorescence marker tdTomato (*18*). SOM-Cre/Ai9 mice, VIP-Cre/Ai9 mice, or PV-Cre/Ai9 mice have SOM^+ interneurons, PV^+ interneurons and VIP^+ interneurons labelling with the fluorescent marker tdTomato respectively. Viatt-Cre was generously provided from Dr. Huda Zoghbi's laboratory. The other Cre and reporter lines were purchased from Jackson Laboratory:

- SOM-Cre: http://jaxmice.jax.org/strain/013044.html
- VIP-Cre: http://jaxmice.jax.org/strain/010908.html
- PV-Cre: http:/jaxmice.jax.org/strain/008069.html
- Ai9 reporter: http://jaxmice.jax.org/strain/007909.html

The visual cortical slice preparation followed previously described methods (*5, 42*), with some additional modifications based on a recently developed NMDG (*N*-Methyl-D-glucamine) recovery slice methods for adults and aging animals (*9, 43*). Briefly, animals were deeply anesthetized using 3% isoflurane. After decapitation the brain was removed and placed into cold (0−4 °C) oxygenated NMDG solution containing 93 mM NMDG, 93 mM HCl, 2.5 mM KCl, 1.2 mM NaH_2PO_4, 30 mM $NaHCO_3$, 20 mM HEPES, 25 mM glucose, 5 mM sodium ascorbate, 2 mM Thiourea, 3 mM sodium pyruvate, 10mM MgSO4 and 0.5 mM $CaCl_2$, pH 7.35. Parasagittal slices were cut from brain tissue with a microslicer (300 μm thick). We took special care to use only parallel slices (i.e. slices that had a cutting plane parallel to the course of the apical dendrites) in order to ensure sufficient preservation of both axonal and dendritic arborizations of neurons in layer 1-5. The brain slices were kept at 37.0 ± 0.5 °C in oxygenated NMDG solution for 10-15 minutes. They were then transferred to the physiological solution (125 mM NaCl, 2.5 mM KCl, 1.25 mM NaH_2PO_4, 25 mM $NaHCO_3$, 1 mM $MgCl_2$, 25 mM glucose and 2 mM $CaCl_2$, pH 7.4) for about 0.5−1 h before starting the recordings. During the recording sessions the slices were submerged in a custom chamber and were stabilized with a fine nylon net attached to a custom designed platinum ring. This recording chamber was continuously perfused with oxygenated physiological solution throughout the recording session.

Electrophysiology

Simultaneous whole-cell *in vitro* recordings from up to eight neurons were obtained from cortical slices as described previously (*5, 42*). We used patch recording pipettes (5−7 MΩ) that were filled with intracellular solution containing 120 mM potassium gluconate, 10 mM HEPES, 4 mM KCl, 4 mM MgATP, 0.3 mM Na_3GTP, 10 mM sodium phosphocreatine and 0.5% biocytin (pH 7.25). We used two Quadro EPC 10 amplifiers for the experiments. A built-in LIH 8+8 interface board was used to perform simultaneous A/D and D/A conversion of current, voltage, command and triggering signals from the amplifiers. The PatchMaster software and custom-written Matlab-based programs were used to operate two Quadro EPC 10 amplifiers and perform online and offline analysis of the electrophysiology data. The eight micromanipulators were mounted on a ring specifically designed for our multi-patching system. Current was injected into the presynaptic neurons (2 nA for 2 ms at 0.01–0.1 Hz) to determine if we could evoke unitary inhibitory or excitatory postsynaptic potentials (uI(E)PSPs) in the putative post-synaptic neurons. The uIPSPs were measured while the membrane potentials of the putative postsynaptic cells were held at −57 ± 3 mV, whereas uEPSPs were measured while membrane potentials of the putative postsynaptic cells were held at −70 ± 4 mV. Recording traces of uI(E)PSPs shown in all figures in the paper are averages of 20−50 consecutive stimulation episodes. These averages were

also used to calculate synaptic latency, 10−90% rise time and decay time constant of evoked uIPSPs or uEPSPs.

We performed recordings from layer 1, layers 2/3 and layer 5 primarily from neurons without obvious apical dendrites in wild-type mice or from labeled neurons in transgenic mice. In each set of recordings one or two pyramidal cells or unlabeled neurons in layers 2/3 and layer 5 were also targeted for recordings. Neurons were assigned to different layers based on the neocortical layer boundaries, which were clearly visible in the micrograph of the bright-field microscope. The layer identity of each neuron was also confirmed post-hoc by reference to nearby morphologically recovered glutamatergic neurons, which have distinct morphology across different layers (*44*). Since neuronal processes can be severed during the slicing procedure (a limitation of all slice electrophysiology experiments), the morphology of neurons and connectivity may be significantly underestimated. However, this is thought to be less of a problem when estimating connectivity between local inhibitory cells (*45*). To improve the morphological integrity of recorded neurons and connectivity rate estimation, we only patch neurons in parallel slices (see above) at depths greater than 15μm from the surface of the slices. We foundthat, with this experimental strategy, the processes of interneurons we recovered rarely stopped abruptly (evidenced by a characteristic retraction ball at the cut ending), even for the long-ranging axons spanning across several cortical layers.

Because the synaptic connectivity significantly depends on the inter-soma distance (Fig.S12A), we took special care to record from groups of neurons with Euclidean inter-soma distances less than 150 μm, for neurons localized within the same layer, and with horizontal distances less than 100 μm for neurons localized in different layers (Fig.S1A). The vast majority of cell pairs within the same layer in our recording sets had an intersoma Euclidean distance of less than 200 μm; the vast majority of the cell pairs localized in different layers had a horizontal distance of less than 150 μm (Fig.S13A). We rarely found synaptic connections, especially inhibitory connections between two neurons within the same layer if they had a Euclidean intersoma-distance of more than 250 μm (Fig.S12B). We also rarely found synaptic connections, especially inhibitory connections, between neurons across layers if their horizontal intersoma-distance was more than 150 μm (Fig.S12C). Therefore, we excluded neuron pairs in the same layer with a Euclidean distance more than 250 μm, and neuron pairs in different layers with a horizontal distance > 150 μm. The inter-soma distances (Euclidean, vertical and horizontal) of cell pairs included for computing the connectivity for each type of connections are not significantly correlated with the connectivity (Fig.S12D), indicating inter-soma distance is not a factor accounting for the connectivity difference we observed in different types of connections (Figs.4A, S14, Supplemental Text).

The recordings were often made in the absence of AMPA and NMDA receptor antagonists, raising the possibility that the identified connections, especially inhibitory connections, could have been polysynaptic. To make sure that the identified connections were monosynaptic, we morphologically confirmed *post hoc* the presynaptic neurons for all connections and made sure that the morphology and electrophysiology of the presynaptic neuron for each connection (i.e. pyramidal neurons vs interneurons) matched the nature of connections (i.e. EPSP vs IPSP). Indeed, the recovered morphology (i.e. pyramidal neurons vs interneurons) and EPSP vs IPSP always matched. Moreover, we measured the latencies of all the connections, and plotted a histogram of the latencies of all inhibitory connections identified in the absence of glutamatergic antagonists and compared it with the histogram of latencies from connections identified in the presence of glutamatergic antagonists (Fig.S11B). If the identified connections were contaminated with polysynaptic events (i.e. longer latencies), the histogram in the absence of glutamatergic antagonists should have had a longer tail compared with the histogram where glutamatergic antagonists were present. However, we found no difference between these two histograms (Fig.S11B). The latencies of uEPSPs (1.89 ±0.08, n=93, Fig.S11C) was within 4 ms, suggesting that all uEPSPs identified in this study were also monosynaptic (*36*). The uEPSPs and uIPSPs were completely abolished by adding glutaminergic antagonists (20 μM CNQX and 100 μM DL-AP5) and PTX (100 μM), respectively.

We calculated the input resistance and membrane time constant of the neurons by injecting long pulses of depolarizing current (300 pA, 600 ms). We measured spike amplitude and afterhyperpolarization (AHP) relative

to the spike threshold. The afterdepolarization (ADP) generally followed a narrow, small AHP that rose above the spike threshold. However, the ADP was also seen as a small depolarization "notch" superimposed onto a bigger, slow AHP, without rising above the spike threshold. The ADPs thus was measured relative to the lowest membrane potential during AHP. Spike-frequency adaptation was calculated as the ratio of the second to the first interspike interval in near-threshold discharges of three or more action potentials and represented as percentage.

Estimation of the proportion of each morphological type

The proportion of each morphologically distinct type in L23 and L5 was estimated based on total labeled L23 and L5 interneurons recorded from Viaat-Cre/ai9 mice since the entire population of GABAergic interneurons in L23 and L5 were labeled with tdTomato (see Main Text). However, the proportions of L1 neurons was not calculated based on the total labeled neurons in L1 because in the Viaat-Cre/ai9 mice a significant number of L1 neurons were unlabeled. Instead, the proportions of L1 interneuron types was estimated based on the total number of randomly recorded L1 neurons from wild type mice.

Morphological reconstructions and analysis.

Morphological recovery and light microscopy examination were carried out according to previously described methods (*5, 42*). Briefly, after the end of the *in vitro* recording experiments, the slices were fixed by immersion in freshly-prepared 2.5% glutaraldehyde/4% paraformaldehyde in 0.1 M phosphate-buffered saline at 4° for at least 48 h. The slices were subsequently processed with the avidin-biotin-peroxidase method in order to reveal the morphology of the neurons. To increase the success rate in recovering the morphology of mature GABAergic interneurons, especially details of their fine axonal arbors, we made several modifications to existing routine biocytin staining protocols. First, we found that a high concentration of biocytin in the internal solution (0.5g/100ml) as well as highly stable micromanipulators are critical for achieving a high recovery rate of cell morphology. Second, each neuron was injected with large depolarizing currents in current clamp mode for fifteen times (100ms, 10-20nA, 1Hz) in order to expedite the diffusion of biocytin into the fine structures. Third, neurons must be recorded for long enough (≥1 hours) to allow the diffusion of biocytin into the very fine axonal structure before being fixed in the freshly-prepared fixation solution. Fourth, the fixed neurons were incubated with avidin-biotin complex and detergents at a high concentration (Triton-X100, 5%) for at least two days before DAB staining. We found that, following all these steps dramatically increased our success rate in recovering the fine axonal arbors of interneurons. The morphologically recovered cells were examined, reconstructed and analyzed using a 100X oil-immersion objective lens and a camera lucida system.

The morphology of each cell was analyzed using the TREES toolbox (*46, 47*) and custom-written software written in our lab. The three-dimensional trees (axon, dendrite and cell body) were converted to two-dimensional planar trees by using the flattening function in the TREES toolbox. For each cell, axonal and dendritic length density (μm per μm^2) were calculated over a grid of 10 × 10 μm elements placed on the corresponding planar trees (*48*). To generate smoother length density maps, the lower resolution maps were interpolated using bi-linear interpolation. Axonal length density maps from different cells (same cell type) were spatially aligned by aligning the origin of each axonal tree. Dendritic length density maps from different cells (same cell type) were spatially aligned by aligning the center of each cell body. The origin of axonal tree and the center of each cell body were assigned spatial coordinate (0, 0) for further analyses. For each type of cell, the axonal (dendritic) length density maps from several cells were averaged and are shown in Fig. S2 (S3), panels A to C. For each cell, a length density projection was obtained by summing length densities from its length density map along a specific direction (horizontal or vertical). For each type of cell, and each direction, axonal (dendritic) length density projections were averaged across several cells and are shown in Fig.S2 (S3), panels D to F.

Principal component analysis and sparse logistic regression classifiers

The 2D axonal and dendritic density maps of a total of 188 fully reconstructed cells (L1: 24, 5 cells only axon; L23: 96; L5: 73) were computed in a grid of 10 × 10 μm. For individual types there were 12.9±3.0 reconstructed cells (mean ± SD; range: 9-18). We convolved both the dendritic as well as axonal maps with a Gaussian kernel with standard deviation 20 μm and computed the first 10 PCA features for each layer , which captured >80% of the variance for all layers and both axons and dendrites. We then used a generalized linear model with binomial link function ('logistic regression') trained with an elastic-net penalty with $\alpha = .95$, resulting in sparse models (*49*). We trained the model to do pairwise classification of neural types within each layer based on the combined 20 axonal and dendritic features. For layer 1, we only used axonal features. Classification performance was evaluated using leave-one-out cross-validation, resulting in a conservative estimate. The regularization strength was chosen using a nested 10-fold cross-validation and the 1-SE-rule. For the classifications in L23 and L5, we counted in how many of the pairwise cell type classification there was significant weight on each feature (weight > 0.01) and ranked the features accordingly. Mostly, the first 3 axonal features were used, giving support to the idea that interneurons can primarily be distinguished based on their axonal features (Fig.S4). The classification performance is shown in Fig.1D.

Statistical analysis.

For analyzing connectivity principles in Fig. 5, we used a generalized linear model (GLM) with a binomial response distribution and a logit link function. We pooled studied connections between all MCs and pyramidal neurons, between NGCs and pyramidal neurons, between all PTIs and pyramidal neurons, and between ISIs and pyramidal neurons for this analysis. Since some connection types contained zeros, we fit the GLM with a weak prior for each combination of factors of p = 0.5, corresponding to adding a positive and a negative outcome for each combination of factors.

Connection probability model

We modeled the number of observed connections between two cell types with a binomial distribution. The underlying connection probability was estimated via maximum a posteriori using a weak beta prior (α = 1.01 and β = 1.01). In the full model, each type of connection in the matrix had its own connection probability. In the restricted models, connection probabilities were shared among certain types. In the uniform model, we used a single connection probability for all types. In the layer model, we used uniform connection probabilities within and between layers. In the model that respects layers and inhibitory or excitatory cells, each group of excitatory and inhibitory neurons within and between layers had their own connection probability. In the master regulator model, we assume the connectivity from NGCs to all neuronal types within the home layer and in nearby layers to be uniform, and the connectivity from MC to every non-MC neuronal type within home layer and in all layers above them to be uniform. We additionally set the connection probability from MCs to themselves to zero. In the ISI model, we assume that L1 SBC-like cells, BPCs and DCs had a same output connection probability parameter to all other interneurons per layer. Connection probabilities of ISIs from and to pyramidal neurons, the connection probabilities to neurons in layers above them, the connections to neurons more than one layer downward (ignoring layer 4), were set to zero. In the PTI model, we modeled each connection probability from BTCs, DBCs, L23BC, ChCs, L5BCs, SCs and HECs to itself with a single parameter. Additionally, the connections from these types to and from pyramidal cells of their home layer had an individual parameter. The likelihood of the entire data is reported in the negative joint log-likelihood (logarithm to base 2) divided by the number of connection types (n = 289). The individual types of connections are assumed to be independent so that the joint likelihood is the sum of the individual likelihoods of the binomial distributions on each type of connections. Error bars on the likelihood depict the standard deviation obtained by bootstrapping Bernoulli trials for each type of connections (50 bootstrap iterations). All plots for the model and the connectivity matrix were created with python's matplotlib library (*50*).

Supplementary Text

Morphology and electrophysiological properties of L123 interneurons

Layer 1 Interneurons

The neurons recorded in L1 (areaV1) of adult mice were morphologically divided into two major types. One type was the neurogliaform cells (NGCs, n = 84), constituting approximately one-third of all L1 neurons (Fig.1E; see Experiment Methods). These neurons had plethora of fine, radiating dendrites that formed roughly symmetrical and spherical dendritic fields (Figs.1A, S3A, S3D). Their axonal geometry was typical of NGCs, as previously described, and their arborization was horizontally elongated and mainly restricted to L1 (Figs.1A, 3A, S2A, S2D, S5A, S6B, S7). This was similar to L1 NGCs reported in juvenile rat somatosensory cortex (*5*). Accordingly, following the previous nomenclature we named them as elongated NGCs (eNGC). Most eNGCs (n = 77/84 neurons) fired late-spiking (LS) action potentials (APs) followed by a deep, wide afterhyperpolarization (AHP; Fig.2A, Type 1; Table S1). Only a small number of eNGCs (n = 7) were not LS (Fig.2A, Type 2). All eNGCs did not have a fast depolarizing "notch" (afterdepolarization: ADP; Fig.2A) following the APs, which was different from other L1 interneurons (see below).

The other major type of L1 neurons typically had longer, more polarized dendritic trees (Figs.1A, 3A, S3A, S3D, S5A, S6B, S7). We also noticed that the axonal arborization of this type of neurons was more varying, compared to the eNGC, but generally followed two major patterns. Many of them (~41%) had a vertically descending axonal bundle, which extended into L5/6 (Figs.1A, S2A, S5A, S6B, S7). This is similar to the single-bouquet cells (SBCs) previously reported in somatosensory cortex (*5, 12*) (classic SBCs). The rest (~59%) had axons that arborized mostly within L1, with only one or two side branches extending to deep layers (not deeper than L4; Figs.1A, 3A, S7) (atypical SBCs). The neurons with these two axonal projection patterns fired APs with marked ADPs and these APs were not delayed in response to near-threshold current injection, and thus were substantially different from the late-spiking of eNGCs (Fig.2A; Table S1). Moreover, some of these cells (~40%) were also capable of burst firing, which we never observed in eNGCs (Fig.2A). Because the non-neurogliaform L1 neurons with the two distinct axonal projection patterns (classic SBC, atypical SBC) shared similar electrophysiological properties (Table S2), dendritic features and connectivity profiles (Table S3), and resemble SBCs in rat somatosensory cortex (*5, 12*) in many perspectives, we grouped them together and named them SBC-like cells.

Layers 2/3 Interneurons

Interneurons from L23 of mature V1 were grouped into seven major types based on morphology: Martinotti cells (L23MCs), neurogliaform cells (L23NGCs), bitufted cells (BTCs), bipolar cells (BPCs), basket cells (L23BCs), double bouquet cells (DBCs) and chandelier cells (ChCs).

L23 Martinotti cell. L23MCs (n = 182) typically had a bitufted somato-dendritic morphology with an elaborate vertically-oriented dendritic tree (Figs.1B, S3B, S3E). Their axons originated from the apical side of the somata or from one of the primary dendrites. The axons ascended toward the pia to form a dense axonal cluster within L1 (Figs.1B, 3A, S2B, S2E, S6A, S6C, S7, S8A, S8C, S9A, S9D, S10). L23MCs with intact firing patterns (n = 172/182) exhibited a firing pattern similar to their young counterparts (*13, 51*). However, these mature L23MCs did not sustain continuous firing in response to prolonged current injection, different from immature MCs (Fig.2B; Table S1). L23MCs were also distinguished from other types of interneurons by their large membrane time constant (Table S1).

L23 Neurogliaform cell. L23NGCs (n = 102) had a dendritic tree similar to that of L1 eNGCs (Figs.1B, S3B, S3E). Their axon could originate from any part of the soma, and shortly after, broke up into a very dense, intertwined and highly ramified arborization of ultra-thin axons (Figs.1B, 3C, S2B, S2E, S6A-B, S7, S8B). Almost all of the L23NGCs with an intact discharge behavior (n = 100/102) were late-spiking (LS). These mature NGCs appeared to have greater frequency accommodation and smaller AHP amplitude (Fig.2B, Table S1) than has been reported in younger animals (*52, 53*).

Bitufted cell. BTCs (n = 118) exhibited a bitufted morphology with two bundles of vertically-oriented dendrites arising from the opposite poles (Figs.1B, 3C, S3B, S3E, S5A, S6C, S7, S9C, S10A-B). Their axon typically originated from the base of the soma and then arborized in to two directions, ascending and descending mostly to neighboring layers, to form a vertically-oriented, roughly symmetrical, tangentially-narrow axonal field (Figs.1B, 3C, S2B, S2E, S5A, S6C, S7, S9C, S10A-B). Their firing patterns were quite variable, and could be grouped into four major types. Of the BTCs with intact discharge behavior, about half (57/101) fired typical irregular-spiking (IS) APs (Type 1, the AP was followed by a slow AHP, which was superimposed by a prominent ADP) with or without an initial burst (Fig.2B, Table S1) (*54, 55*). Seventeen out of 101 BTCs (16.8%) also discharged irregularly, but their APs were followed by a deeper and faster AHP than in typical IS, and were not followed by an ADP (Type 2, Fig.2B). Twenty-two out of 101 BTCs (21.7%) had a discharge pattern very similar to MCs (Type 3, Fig.2B). A small number of BTCs (n = 5) discharged regularly in response to sustained depolarizing currents (Type 4, Fig.2B).

Bipolar cell. BPCs (n = 85) were small, ovoid cells with narrow bipolar dendrites extending upwards to L1 and downwards to L5 and L6 (Figs.1C, S3B, S3E). The ascending dendrite had elaborate branches in L1, resembling the apical dendrites of pyramidal neurons (Figs.1C, 3C, S3B, S3E, S5A, S6B, S7, S8B, S9C, S10B). The axon emerged from one of the primary dendrites and formed a narrow descending band that typically reached L6 (Figs.1C, 3C, S2B, S2E, S5A, S6B, S7, S8B, S9C, S10B). All recovered BPCs with intact discharge behaviors were IS with (Type 1, ~40%; 29 out of 75) or without (Type 2, 60%; 46 out of 75) initial burst (Fig.2B). BPCs also had lower resting membrane potentials and larger AP amplitudes than other types of interneurons (Table S1).

Double bouquet cell. DBCs (n = 46) had a narrow, vertically-oriented, bitufted dendritic tree (Figs.1C, 3A, S3B, S3E, S6A, S7 and S8C). Their axons typically originated from the base of the somata and descended toward the deeper layers. Along the descending path it frequently bifurcated into branches, which either ascended or descended vertically, thus forming a narrow fascicular axonal structure extending across all layers (Figs.1C, 3C, S2B, S2E, S6A, S7 and S8C). All recovered DBCs with intact discharge behaviors (n = 43) had a fast-spiking (FS) firing pattern (Fig.2B, Table S1).

L23 basket cell. L23BCs (n = 322) were the most abundant interneuron type encountered in L23 of mature V1 (Fig.1E). These neurons had large somata and typically a vertically-oriented, bitufted-like dendritic tree, although horizontally-oriented dendrites were also occasionally observed (Figs.1C, 3B, S3B, S3E, S7, S8A, S8D, S9A, S9E, S10A-B). They had very thick axons, which originated from the apical side of the somata and ascended toward L1 for a variable distance before bifurcating into several major branches. These branches then arborized extensively around the somata, with a few higher-order branches extending horizontally into neighboring columns and vertically into L5 and L6 (Figs.1C, 3B, S2B, S2E, S7, S8A, S8D, S9A, S9E, S10A-B). All recovered BCs with intact discharge behaviors (n = 314/322) were FS (Fig.2B, Table S1). L23BCs we recovered were highly homogeneous, and we did not observe any non-FS BC that are believed to be cholecystokinin-expressing (CCK^+) and have physiological and morphological features distinct from FS BCs (*56-58*). The non-FS BCs have been shown to be present in rat somatosensory cortex and prefrontal cortex (*56, 57*), but we did not observe this type of interneurons in adult mouse visual cortex, suggesting that interneuron cell types vary across brain regions and may be species-specific (*59, 60*).

Chandelier cell. ChCs (n = 18) were easily distinguished by their candlestick-like axonal structure (Figs.1C, S8B). They also had characteristic asymmetric, narrow dendritic trees with most branches ascending toward the pia (Figs.1C, S3B, S3E, S8B). All recovered ChCs with intact discharge behaviors (n = 15) were FS (Fig.2B, Table S1).

Output connectivity profiles

Layer 1 Interneurons

L1 neurons in mature V1 had output connection patterns similar to their counterparts in the developing cortex (*5*). SBC-like cells rarely connected to pyramidal neurons and to other L1 neurons (Figs.3A, 3C, S5A, S6B, S14, and Table S3). In contrast, eNGCs inhibited L23 and L5 pyramidal neurons (Figs.3A, S14), and both types of L1 neurons (connection probability to eNGCs p = 55.1%, 16/29 pairs, uIPSPs amplitude (Amp): 1.64 ± 0.44 mV; to SBC-like cells: p = 65.6%, 21/32 pairs, Amp: 1.87 ± 0.47 mV; Figs.3A, S5A, S6B, S14, Table S6).

Both eNGCs and SBC-like cells inhibited L23 interneurons, but not L5 interneurons (Fig.S14). SBC-like cells preferentially projected to ChCs (p = 21.4%, 6/28 pairs, Amp: 0.47 ± 0.16 mV), BTCs (p = 17.1%, 6/35 pairs, Amp: 0.62 ± 0.20 mV) and BPCs (p = 20.9%, 4/20 pairs, Amp: 0.80 ± 0.24 mV; Fig.S14, Table S6). eNGCs preferentially projected to L23NGCs (p = 35.5 %, 11/31 pairs, Amp:1.04 ± 0.31 mV; S6B, S14), BTCs (p = 45.4%, 20/44 pairs, Amp:0.92 ± 0.15 mV; Figs.S5A, S14) and BPCs (p = 47.6%, 10/21 pairs; Amp: 1.03 ± 0.23 mV; Figs.S5A, S6B, S14; Table S6).

Layers 2/3 Neurons

L23 Martinotti Cell. L23MCs avoided inhibiting other L23MCs (p = 0.0%, 0/130), but highly innervated all other neuronal types in L1 and L23, including L23 pyramidal neurons (L23Pyr) (connectivity rates ranged from 41% to 50% for all cell types; Figs.3A, S6A, S6C, S8A, S8C, S9A, S14; Table S6). L23MCs also projected to L5 pyramidal neurons (L5Pyrs) with a low connection probability (p = 8.1%, 6/74 pairs, Amp: 0.22 ± 0.06 mV), and rarely to L5NGCs (p=4.5%, 1/22 pairs) and L5BCs (p = 5.0%; 2/40 pairs, Amp: 0.23 ± 0.00 mV; Fig.S14, Table S6).

L23 Neurogliaform Cell. Single APs in L23NGC elicited slow, large-amplitude uIPSPs in almost all simultaneously recorded neurons, regardless of cell type or layer. Inhibitory projections from L23NGCs are highest and strongest in L1 and L23 (connectivity rate ranged from 47.5% to 65.2%; Figs.3C, S6A-B, S8B, S14; Table S6), and modest in L5 (connectivity rate ranged from 25.0% to 35.5%; Figs.3C, S14; Table S6).

Bitufted Cell. BTCs preferentially projected to L23MCs (p = 26.1%, 12/46 pairs, Amp: 0.32 ± 0.05 mV), but they also projected to L23Pyrs (p = 18.3%, 11/60 pairs, Amp: 0.29 ± 0.11 mV), to other BTCs (p = 14.4%, 8/56 pairs, Amp: 0.44 ± 0.08 mV) and to BPCs (p = 9.1%, 5/55 pairs, Amp: 0.30 ± 0.10 mV; Figs.S6C, S14; Table S6). Notably, no connection was identified from BTCs to any cell type in L1 or L5 (Fig.S14).

Bipolar Cell. BPCs specifically projected to L5MCs (p = 31.0%, 9/29 pairs; Amp: 0.30 ± 0.07 mV; Figs.S5A, S14; Table S6). Connections to other cell typees in L1, L23 or L5 were exceedingly rare (p < 0.1%, 1/531 pairs, for all cell types combined; Figs.3C, S5A, S6B, S8B, S14).

Double Bouquet Cell. DBCs primarily inhibited other DBCs (p = 44.7%, 17/38 pairs, Amp: 0.77 ± 0.14 mV) and L23Pyrs (p = 39.4%, 13/33 pairs, Amp: 0.52 ± 0.12 mV) (Figs.3A, S8C), but also projected to L23BCs (p = 18.1%, 8/45 pairs, Amp: 0.72 ± 0.15 mV), BPCs (p = 21.4%, 3/14 pairs, Amp: 0.52 ± 0.21 mV) and L5Pyrs (p = 13.5%, 5/37 pairs, Amp: 0.25 ± 0.06 mV; Fig.S14; Table S6). No connection was identified from DBCs to any cell type of L1 or L5 interneurons (Fig.S14).

L23 Basket Cell. L23BCs primarily inhibited other BCs (p = 46.8%, 168/359 pairs, Amp:0.69 ± 0.05 mV for L23BCs; p = 13.6%, 15/110 pairs, Amp: 0.79 ± 0.18 mV for L5BCs) and Pyrs (p = 35.2%, 75/213 pairs, Amp: 0.50 ± 0.06 mV for L23Pyrs; p = 5.9%, 11/185 pairs, Amp: 0.20 ± 0.02 mV for L5Pyrs; Figs.3B, S8A, S14), but also projected to L23MCs (p = 18.2%, 16/88 pairs, Amp: 0.42 ± 0.10 mV, Figs.S8A, S9A), DBCs (p = 13.3%, 6/45 pairs, Amp: 0.69 ± 0.14 mV), BTCs (p = 11.4%, 8/70 pairs, Amp: 0.41 ± 0.08 mV), ChCs (p = 13.3%, 3/22 pairs, Amp: 0.69 ± 0.26 mV) and BPCs (p = 4.3%, 2/47 pairs, Amp: 0.41 ± 0.05 mV; Fig.S14; Table S6).

Chandelier Cell. ChCs were encountered very rarely in visual cortex of adult mice compared to other interneuron types (Fig.1E). Based on the limited number of connections tested, ChCs appeared to project exclusively to other ChCs (p = 37.5%, 6/16 pairs, Amp: 0.47 ± 0.14 mV) and to L23Pyrs (p = 31.3%, 5/16 pairs, Amp: 0.35 ± 0.03 mV; Figs.S8B, S14; Table S6).

L23 Pyramidal Cell. L23Pyrs projected to MCs (p = 18.9%, 20/106 pairs, Amp:1.19 ± 0.26 mV for L23MCs; p = 11.2%, 10/89 pairs, Amp:0.53 ± 0.12 mV for L5MCs; Figs.S9A, S9D, S14; Table S6) with uEPSPs that were facilitating (second uEPSP/first uEPSP [Amp ratio]: 264 ± 35%, n=10 for L23MCs; 151 ±

11%, n = 8 for L5MCs; Figs.S9A,S9D, S9F), to BCs (p = 18.6%, 41/211 pairs, Amp: 1.61±0.22 mV for L23BCs; p = 7.9%, 5/63 pairs, Amp: 1.32 ± 0.20 mV for L5BCs; Figs.S9A-B, S14; Table S6) with uEPSPs that were weakly depressing (Amp ratio: 74 ± 6%, n = 14 for L23BCs; 82 ± 4%, n = 4 for L5BC; Figs.9A-B, S9F), to BTCs (p = 20.0%, 12/60 pairs, Amp: 1.31 ± 0.32mV; Figs.S9C, S14; Table S6) with uEPSPs that were strongly depressing (Amp ratio: 45 ± 10%, n = 10; Fig.S9F), and to HECs (p = 7.5%, 3/40 pairs, Amp: 1.15 ± 0.28mV; Fig. S14) with uEPSPs that were modestly depressing (Amp ratio: 60 ± 20%, n = 3; Fig.S9F). No connection from L23Pyr to the remaining types of interneurons was identified (Fig.S14). L23Pyrs also projected to L5Pyrs (p = 4.0%, 6/149 pairs, Amp: 1.13 ± 0.35mV), but connection probability among L23Pyrs was very rare (p = 1.8%, 2/112 pairs), which appears to be lower than previous reports (*61*). This low connectivity may be due to a large range of inter-soma distances between tested L23Pyrs (Fig.13B, average distance: 102 ± 4 μm), or was related to the age of the animals tested.

Layer 5 Neurons

L5 Martinotti Cell. L5MCs projected to all interneuron cell types in L1, L23 and L5 with a similar connection probability (Connectivity range: 25%-36%; Figs.3A, S5A, S5D, S8B, S14; Table S6), except to other MCs, which they avoided (p = 0.0%, 0/133 pairs for L23MCs; p = 0.0%, 0/92 pairs for L5MCs; Figs.3A, S14). The connectivity from L5MCs to pyramidal neurons was slightly lower than to other cell types (Fig.S14), but in light of the fact that pyramidal neurons have a larger and more sophisticated dendritic tree than interneurons, this could reflect missed connections. Since MCs primarily synapse on the terminal region of the apical dendrite of pyramidal neurons (*62*), the local unitary inhibitory events evoked by MCs are highly compartmentalized and far away from the soma and could be significantly attenuated by the time they reach the soma (*63*). Thus, those small events in tuft region may have never reached the soma and were missed. Consistent with this explanation, we found that the connection strength from MCs to pyramidal neurons tended to be lower than the strength from MCs to other interneurons (Table S6). Therefore, MCs likely projected to both pyramidal neurons and non-MC interneurons in a non-selective manner (Fig.6B).

L5 Neurogliaform Cell. Stimulation of L5NGCs elicited slow uIPSPs with large amplitudes in almost all simultaneously recorded neurons (Fig.3C), similar to L23NGCs. Inhibitory projections from L5NGCs were highest and strongest in L5 (Connectivity rate range: 54.5%-66.7%; Figs.3C, S14; Table S6), and moderate in L23 (connectivity rate range: 27.3%-33.3%; Figs.3C, S14; Table S6). There was no connection identified from L5NGCs to L1 neurons (Fig.S14).

L5 Basket Cell. L5BCs mostly inhibited other BCs (p = 47.8%, 32/67 pairs, Amp: 1.19 ± 0.18 mV for L5BCs; p = 21.4%, 22/103 pairs, Amp: 0.51 ± 0.11 mV for L23BCs) and pyramidal neurons (p = 25.0%, 33/132 pairs, Amp: 0.81 ± 0.16 mV for L5Pyrs; p = 10.1%, 7/69 pairs, Amp: 0.35 ± 0.16 mV for L23Pyrs) (Figs.3B, S5D, S14), and also inhibited other L5 cells: L5MCs (p = 15.8%, 12/76 pairs, Amp: 0.46 ± 0.11 mV; Fig.S5D, S14), L5NGCs (p = 15.0%, 3/20 pairs, Amp: 0.17 ± 0.03 mV), SCs (p = 12.5%, 4/32 pairs, Amp: 0.60 ± 0.17 mV) and HECs (p = 3.8%, 1/26 pairs; Fig.S14; Table S6).

Shrub Cell. SCs mainly targeted other SCs (p = 62.5%, 15/24 pairs, Amp: 1.24 ± 0.29 mV; Fig.S5B), but also inhibited L5Pyrs (p = 9.8%, 5/51 pairs, Amp: 0.46 ± 0.09 mV; Fig. S14; Table S6). No connection was identified from SC to any type of L1 and L23 neurons (Fig.S14).

Horizontally Elongated Cell. HECs exclusively inhibited other HECs (p = 50.0%, 11/22 pairs, Amp: 0.81 ± 0.26 mV) and L5Pyrs (p = 30.2%, 16/53 pairs, Amp: 0.84 ± 0.21 mV; Figs.S5C, S14; Table S6).

Deep-Projecting Cell. The only post-synaptic targets of DCs were L5MCs (p = 8.3%, 2/24 pairs, Amp: 0.30 ± 0.02 mV; Fig. S14). Since the axons of these cells could reach L6, it was possible that DCs targeted additional cell types from which we did not record.

L5 Pyramidal Cell. L5Pyrs projected to L5MCs (p = 7.8%; 8/102 pairs, Amp: 0.48 ± 0.09mV, Figs. S9E, S14) with facilitating synapses (Amp ratio: 265 ± 37%, n = 5; S9F), and to L5BCs (p = 11.3%, 13/115 pairs, 1.20 ± 0.12 mV; Figs.S5D, S14) and HECs (p = 16.7%, 8/48 pairs, Amp: 0.52 ± 0.07 mV; Figs.S5C, S14) with weakly depressing synapses (Amp ratio: 85 ± 5%, n = 7 for L5BC; 87 ± 3%, n = 5 for HEC; S9F). L5Pyrs also

projected to L23BCs (p = 2.9%, 5/173 pairs, Amp: 1.08 ± 0.30 mV; Figs.S9E, S14), L23NGCs (p = 2.7%, 2/74 pairs; Fig.S14) and eNGCs (p = 1.7%, 1/60 pairs; Fig.S14). No connection was identified among L5Pyrs (Fig.S14). We believe the low connectivity among L5Pyrs was related to the age of the animals tested because we found that the connectivity among L5Pyrs in juvenile slices within the same range of intersoma-distance (Fig. S13B, average: 91±4μm) was comparable with reports from other groups (*36, 37*).

Layer 5 pyramidal neurons could be differentiated into two types with a slight morphological difference: slender-tufted and thick-tufted (Fig.S7C-F), and these two types of neurons have been shown to differ from each other in the brain regions they project to (*64*). Nevertheless, connectivity of these two types of pyramidal neurons with interneurons is similar (Table S10), and we thus pooled them together for our analysis.

Input connectivity profiles

Almost all cell types received inputs from NGCs and MCs, indicating these two types of interneurons provided non-specific inhibitory sources for local microcircuits (Figs.4, S14). Some cell types also received specific inhibitory inputs.

Layer 1 Interneurons

Except from non-specific inhibitory inputs (L23MC, L5MC, L1 eNGC and L23NGC), L1 neurons rarely received inhibition from other types of interneurons, nor excitatory inputs from L23pyrs and L5pyrs (Figs.4, S14).

Layer 2/3 Interneurons

L23 Martinotti Cell. Besides non-specific inhibition (L23 and L5 NGCs), L23MCs were exclusively inhibited by BTCs and L23BCs. They could be easily driven by L23Pyrs, but not L5Pyrs (Figs.4, S14).

L23 Neurogliaform Cell. L23NGCs received no specific inhibitory inputs. They were not innervated by L23Pyrs, but were weakly innervated by L5Pyrs (Figs.4, S14).

Bitufted Cell. Besides non-specific inhibitory inputs (MCs and NGCs in different layers), BTCs received inputs from SBC-like cells, other BTCs, L23Pyrs and L23BCs (Figs.4, S14).

Bipolar Cell. Besides non-specific inhibition, BPCs received inhibition from SBC-like cells, BTCs and DBCs. BPCs rarely received excitatory inputs from L23Pyrs and L5Pyrs (Figs.4, S14).

Double Bouquet Cell. Besides non-specific inhibition, DBCs received inhibition exclusively from other DBCs and L23BCs (Figs.4, S8C, S14). DBC rarely received excitatory inputs from L23Pyrs and L5Pyrs (Figs.4, S14).

L23 Basket Cell. Besides non-specific inhibitory inputs, L23BCs received inhibitory inputs from other BCs (both L23 and L5) and DBCs, and excitatory inputs from both L23Pyrs and L5Pyrs (Figs.4, S14).

Chandelier Cell. Besides non-specific inhibitions, ChCs received inhibitions from other ChCs and L23BCs (Figs.4, S14).

L23 Pyramidal Cell. Besides non-specific inhibition, L23Pyrs received inhibitions from BCs (both L23 and L5), DBCs, BTCs and ChCs (Figs.4, S14).

Layer 5 Neurons

L5 Martinotti Cell. Besides non-specific inhibitory inputs (NGCs), L5MCs received inhibitory inputs from BPCs and L5BCs, and excitatory inputs from both L23Pyrs and L5Pyrs (Figs.4, S14).

L5 Neurogliaform Cell. Besides non-specific inhibition, L5NGCs were weakly innervated by two types of L5 fast-spiking neurons, namely L5BCs and SCs. L5NGCs rarely received excitatory inputs from L23Pyrs and L5Pyrs (Figs.4, S14)

L5 Basket Cell. Besides non-specific inhibition, L5BCs received inhibition exclusively from other BCs (L23 and L5), and excitatory inputs from both L23Pyrs and L5Pyrs (Figs.4, S14).

Shrub Cell. Besides non-specific inhibition, SCs received inhibition mainly from other SCs, and a small amount of inhibition from L5BCs. SCs rarely received excitatory inputs from L23Pyrs and L5Pyrs (Figs.4, S14).

Horizontally Elongated Cell. Besides non-specific inhibition, HECs received inhibition mainly from other HECs, and to a much lower extent, from L5BCs. HECs could be driven by both L23Pyrs and L5Pyrs (Figs.4, S14).

Deep-Projecting Cell. Except for non-specific inhibitory inputs, DCs rarely received inputs from local microcircuits (Figs.4, S14).

L5 Pyramidal Cell. Beside non-specific inhibition, L5Pyrs received inhibitions from BCs, SCs, HECs and DBCs. L5Pyrs were mainly driven by L23Pyrs (Figs.4, S14).

Fig.S1

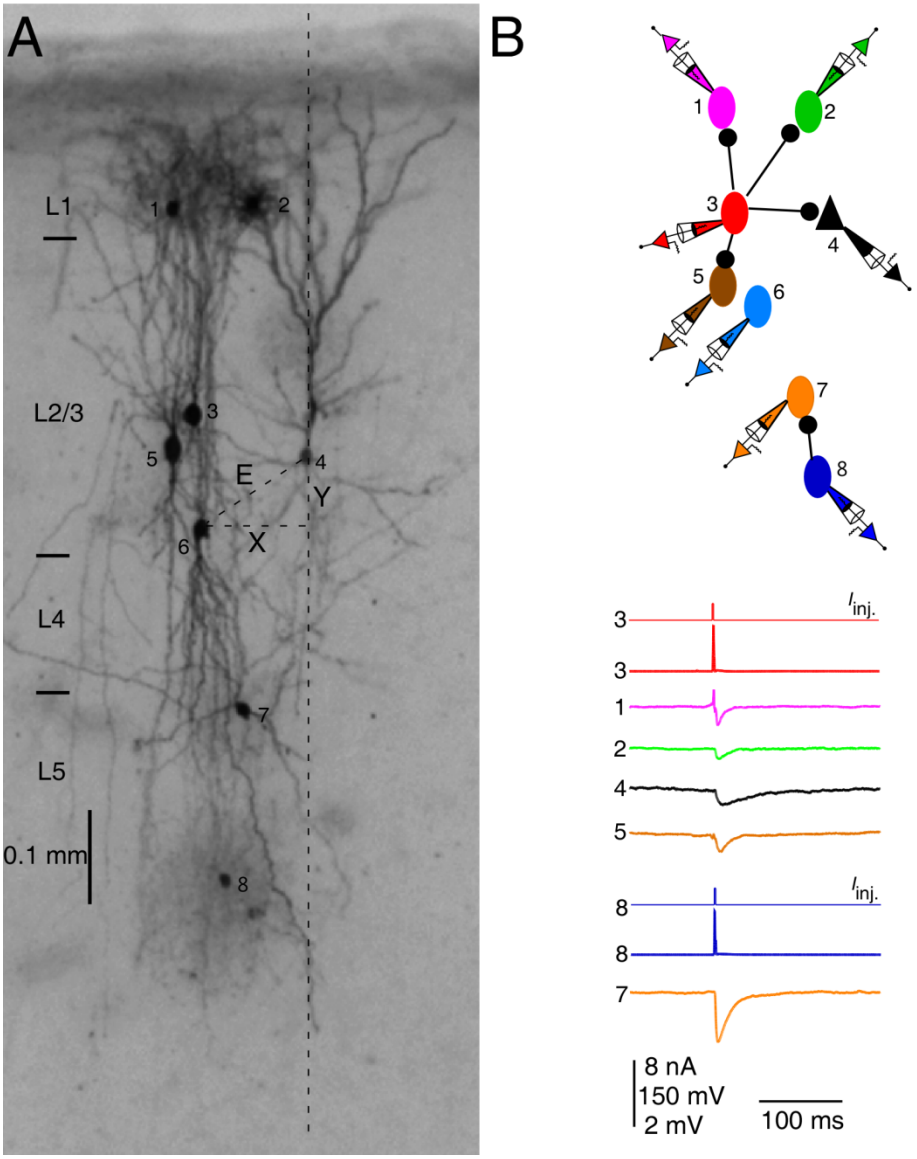

Fig. S1. Simultaneous octuple whole-cell recording configuration and pair-wise connectivity. (**A**) Morphological recovery of a cluster of eight neurons recorded simultaneously from L1, L23 and L5. Recorded neurons were close to each other in the horizontal distance (X) (generally less than 100μm). (**B**) Connection diagram of eight neurons in A. Each of eight neurons was stimulated and the responses of the remaining neurons were monitored. Single action potentials (APs) elicited in cell 3 and cell 8 evoked uIPSPs in cell 1, 2, 4, 5 and cell 7 respectively. No connection was identified from cell 1, cell 2, cell 4, cell 5, cell 6 and cell 7 (traces not shown). Vertical scale bar shows, from top to bottom, amplitudes of current injection (I_{inj} in nA), APs (mV), uIPSPs (mv)..

Fig. S2

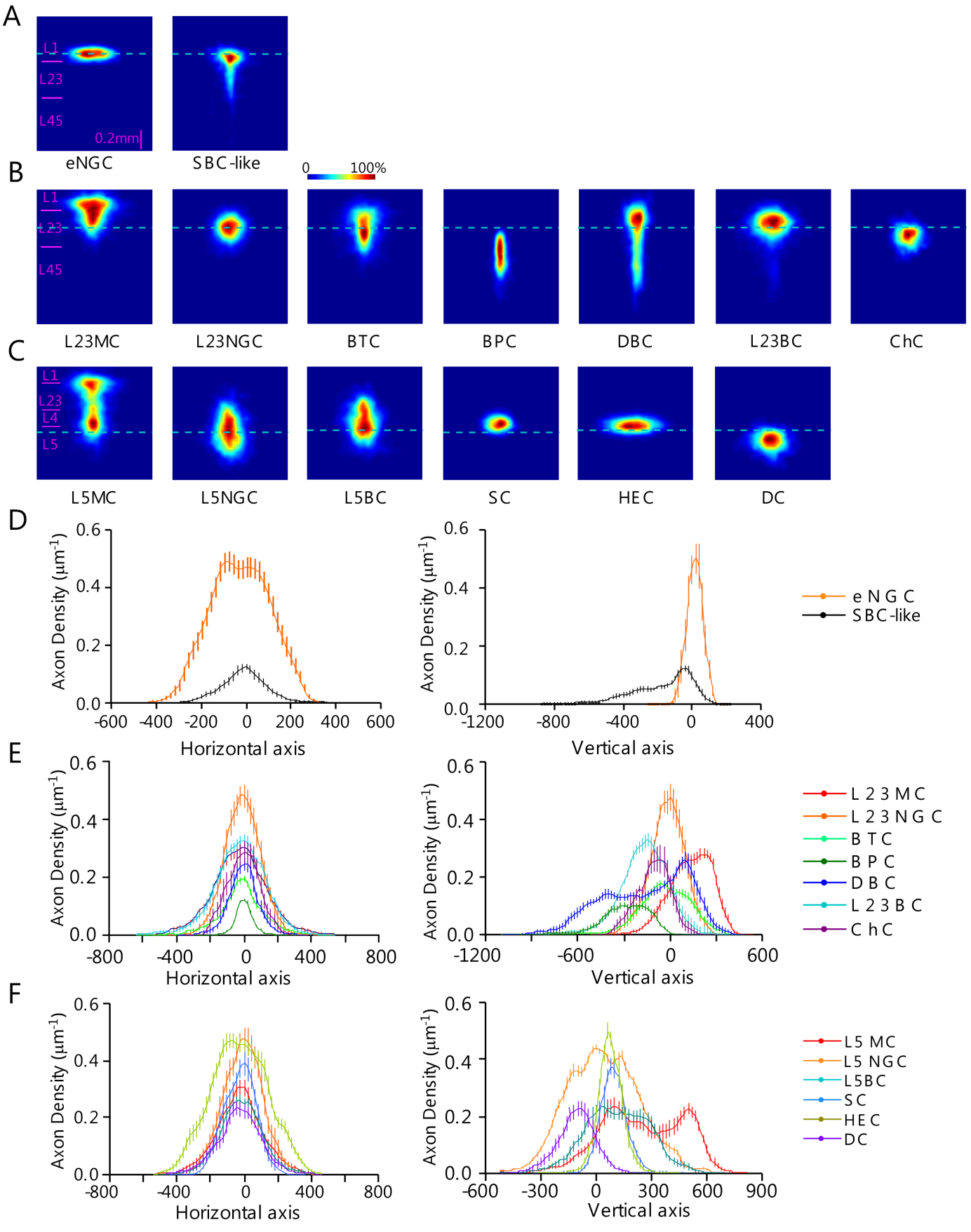
A
L1
L23
L45
0.2mm
eNGC
SBC-like
0
100%
B
L23MC
L23NGC
BTC
BPC
DBC
L23BC
ChC
C
L1
L23
L4
L5
L5MC
L5NGC
L5BC
SC
HEC
DC
D
Axon Density (μm-1)
Horizontal axis
Vertical axis
eNGC
SBC-like
E
L23MC
L23NGC
BTC
BPC
DBC
L23BC
ChC
F
L5MC
L5NGC
L5BC
SC
HEC
DC

Fig.S2. Axonal length density heat maps of L1-5 interneurons. (**A**) Axonal length density heat maps of L1 interneurons (eNGCs: n=12; SBC-like cells: n=15); (**B**) Axonal length density heat maps of L23 interneurons (L23MCs: n=17; L23NGCs: n=16; BTCs: n=26; BPCs: n=17; DBCs: n=11; L23BCs: n=14; ChCs: n=9); (**C**) Axonal length density heat maps of L5 interneurons (L5MCs: n=18; L5NGCs: n=10; L5BCs: n=15; SCs: n=10; HECs: n=12; DCs: n=11). The center of the dash lines indicates the origin of axons. (**D**) Axonal length density plots at both the horizontal and vertical axes of L1 neurons (eNGCs: n=12; SBC-like cells: n=15); (**E**) Axonal length density plots at both the horizontal and vertical axes of L23 interneurons (L23MCs: n=17; L23NGCs: n=16; BTCs: n=26; BPCs: n=17; DBCs: n=11; L23BCs: n=14; ChCs: n=9); (**F**) Axonal length density plots at both the horizontal and vertical axes of L5 interneurons (L5MCs: n=18; L5NGCs: n=10; L5BCs: n=15; SCs: n=10; HECs: n=12; DCs: n=11). Zero on the axes indicates the origin of the axons (positive direction of the vertical axis points towards the pia). Error bars represent s.e.m. For each cell, single features were derived from the line length density map using principal component analysis for cross-validated sparse logistic regression classifiers (Fig.S4).

Fig. S3

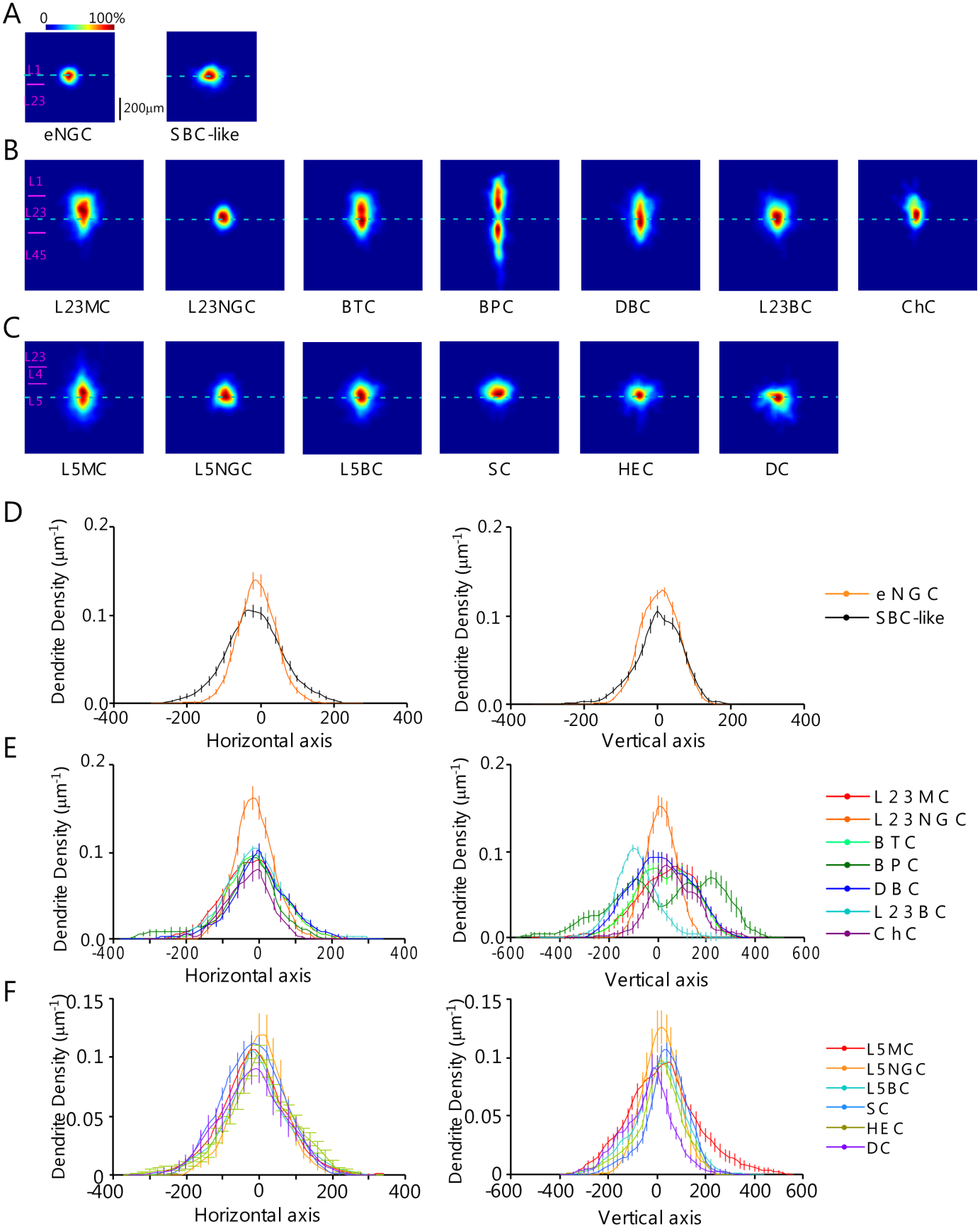
A
0
100%
L1
L23
200μm
eNGC
SBC-like
B
L1
L23
L45
L23MC
L23NGC
BTC
BPC
DBC
L23BC
ChC
C
L23
L4
L5
L5MC
L5NGC
L5BC
SC
HEC
DC
D
Dendrite Density (μm-1)
Horizontal axis
Vertical axis
eNGC
SBC-like
E
L23MC
L23NGC
BTC
BPC
DBC
L23BC
ChC
F
L5MC
L5NGC
L5BC
SC
HEC
DC

Fig.S3. Dendritic length density heat maps of L1-5 interneurons. (**A**) Dendritic length density heat maps of L1 interneurons (eNGCs: n=15; SBC-like cells: n=20); (**B**) Dendritic length density heat maps of L23 interneurons (L23MCs: n=16; L23NGCs: n=16; BTCs: n=26; BPCs: n=17; DBCs: n=15; L23BCs: n=18; ChCs: n=8); (**C**) Dendritic length density heat maps of L5 interneurons (L5MCs: n=24; L5NGCs: n=8; L5BCs: n=19; SCs: n=17; HECs: n=14; DCs: n=9). The center of the dash lines indicates the center of the somata. (**D**) Dendritic length density plots at both the horizontal and vertical axes of L1 neurons (eNGCs: n=15; SBC-like cells: n=20); (**E**) Dendritic length density plots at both the horizontal and vertical axes of L23 interneurons (L23MCs: n=16; L23NGCs: n=16; BTCs: n=26; BPCs: n=17; DBCs: n=15; L23BCs: n=18; ChCs: n=8); (**F**) Dendritic length density plots at both the horizontal and vertical axes of L5 interneurons (L5MCs: n=24; L5NGCs: n=8; L5BCs: n=19; SCs: n=17; HECs: n=14; DCs: n=9). Zero on the axes indicates the center of the soma (positive direction of the vertical axis points towards the pia). Error bars represent s.e.m. For each cell, single features were derived from the line length density map using principal component analysis for cross-validated sparse logistic regression classifiers (Fig.S4).

S4

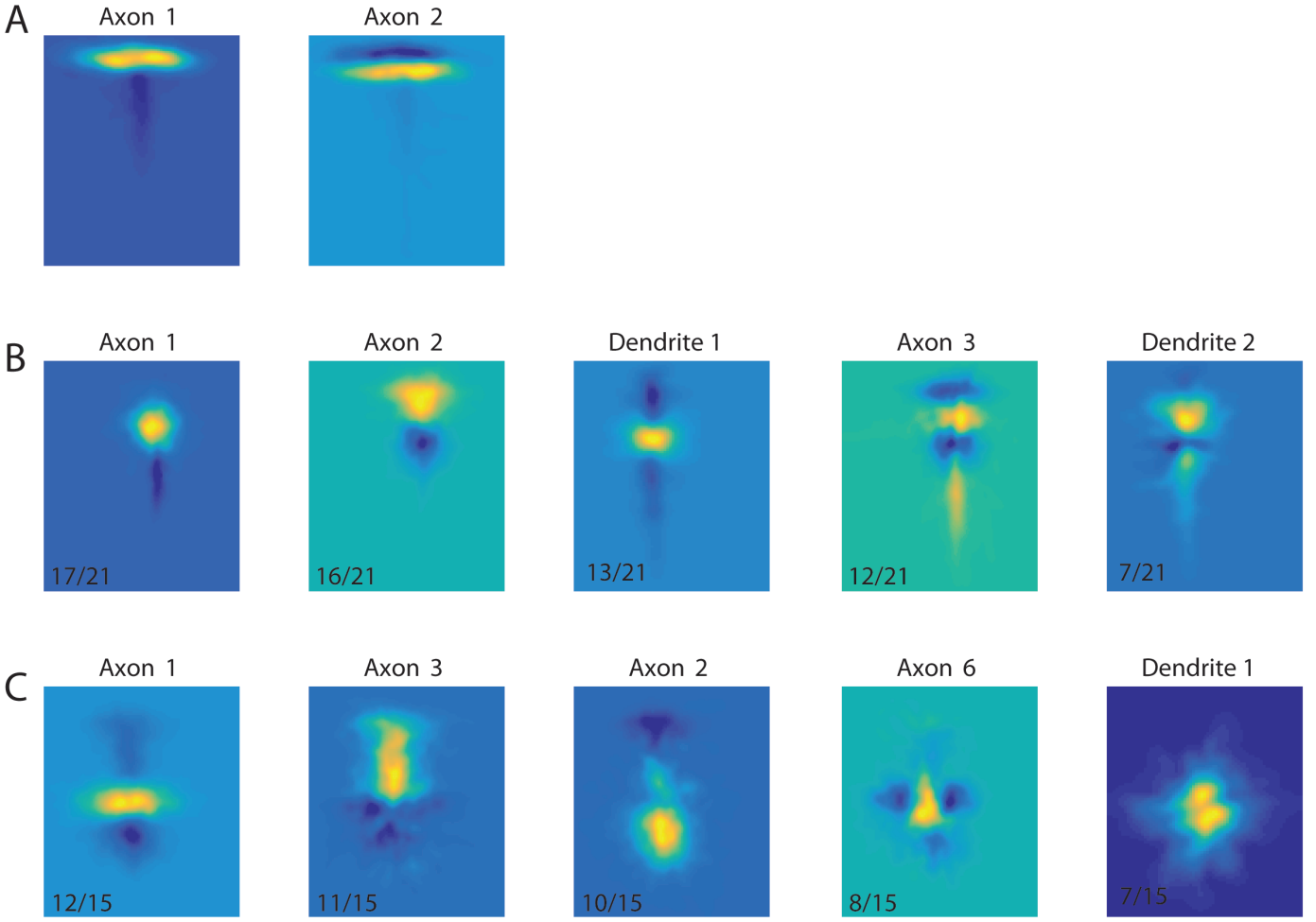
A
Axon 1
Axon 2
B
Axon 1
Axon 2
Dendrite 1
Axon 3
Dendrite 2
17/21
16/21
13/21
12/21
7/21
C
Axon 1
Axon 3
Axon 2
Axon 6
Dendrite 1
12/15
11/15
10/15
8/15
7/15

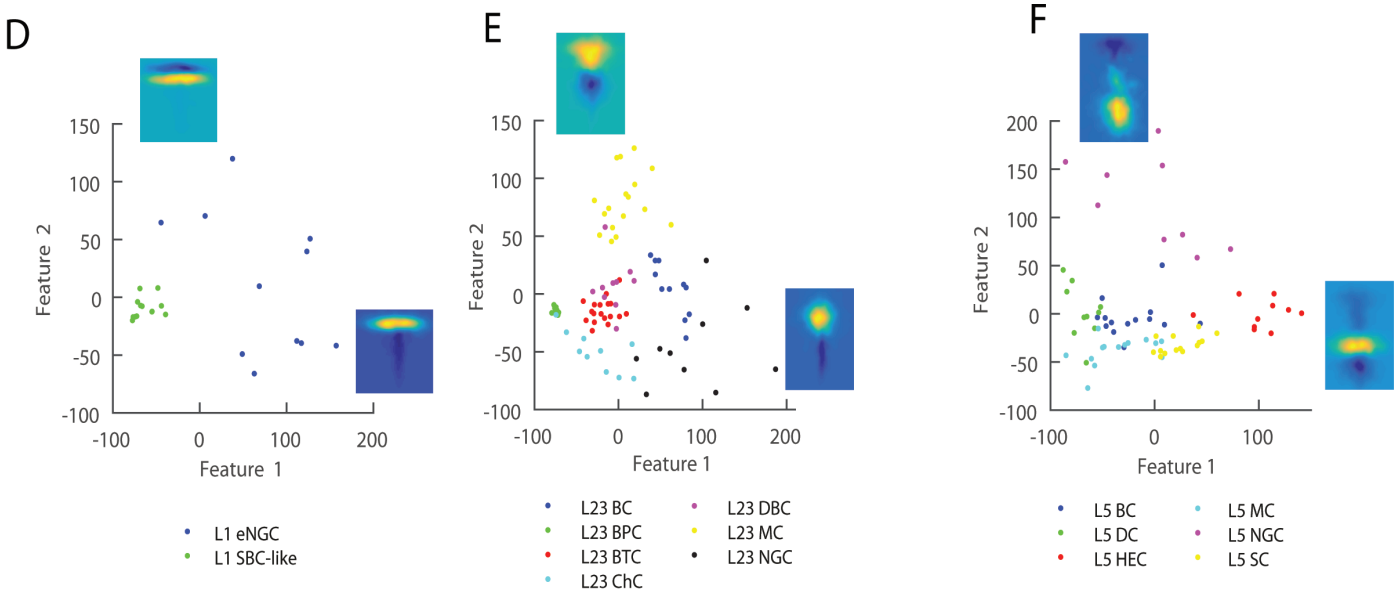
D
Feature 2
Feature 1
L1 eNGC
L1 SBC-like
E
Feature 2
Feature 1
L23 BC
L23 BPC
L23 BTC
L23 ChC
L23 DBC
L23 MC
L23 NGC
F
Feature 2
Feature 1
L5 BC
L5 DC
L5 HEC
L5 MC
L5 NGC
L5 SC

Fig.S4. Axonal and dendritic features computed using PCA from the axon and dendrite density map of interneurons of each layer used in the classification analysis (A-C) and the scatter plots of all types for axonal features 1 and 2 (D-F). For L23 and L5, the features are ranked by the number of times they were used in pairwise classification of cell types with a weight >0.01. For L1, mainly axonal feature 1 was used. (**A**) Features of L1 neurons; (**B**) Features of L23 interneurons; (**C**) Features of L5 interneurons. (**D**) Scatter plot of L1 neurons for axon features 1 and 2; (**E**) Scatter plot of L23 interneurons for axon features 1 and 2; (**F**) Scatter plot of L5 interneurons for axon features 1 and 2.

Fig.S5

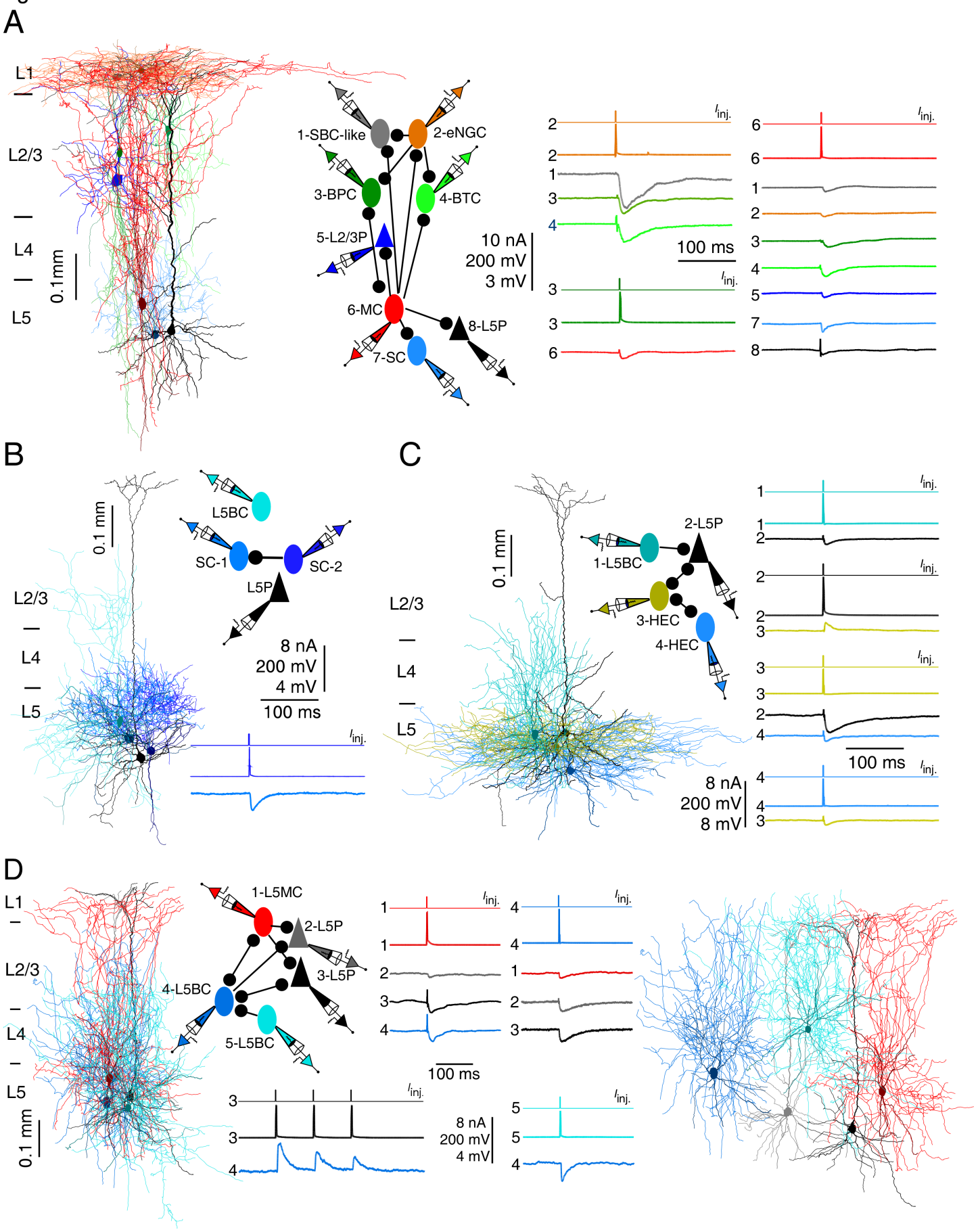
A
L1
L2/3
L4
L5
0.1mm
1-SBC-like
2-eNGC
3-BPC
4-BTC
5-L2/3P
6-MC
7-SC
8-L5P
10 nA
200 mV
3 mV
100 ms
B
0.1 mm
L2/3
L4
L5
L5BC
SC-1
SC-2
L5P
8 nA
200 mV
4 mV
100 ms
C
0.1 mm
L2/3
L4
L5
2-L5P
1-L5BC
3-HEC
4-HEC
100 ms
8 nA
200 mV
8 mV
D
L1
L2/3
L4
L5
0.1 mm
1-L5MC
2-L5P
3-L5P
4-L5BC
5-L5BC
100 ms
8 nA
200 mV
4 mV

Fig.S5. Connection between morphologically distinct typees of interneurons in V1. Vertical scale bars not showing distance show, from top to bottom, amplitudes of current injection (I_{inj} in nA), APs (mV), uIPSPs (mV). (**A**) Connections between eight simultaneously recorded neurons including one eNGC, one SBC-like cell, one BTC, one BPC, one L23Pyr, one L5Pyr, one L5MC and one SC (Left). Each neuron was spatially separated in Fig.S7D. Middle: connection diagram of eight reconstructed neurons**.** Right: Single APs elicited in eNGC (cell 2) evoked uIPSPs in SBC-like cell, BPC and BTC, not in other neurons; APs elicited in BPC (cell 3) evoked uIPSPs only in L5MC; APs elicited in L5MC (cell 6) evoked uIPSPs in all other neurons. (**B**) Connections between four simultaneously recorded, morphologically reconstructed L5 neurons including two SCs, one L5BC and one L5Pyr (Left). Each neuron was spatially separated in Fig.S7E. Right: connection diagram of four neurons**.** Single APs in one SC (SC-2) evoked uIPSPs in another SC (SC-1), but not in other neurons. (**C**) Connections between four simultaneously recorded L5 neurons including two HECs, one L5BC and one L5Pyr (Left). Each neuron was spatially separated in Fig.S7F. Right: connection diagram of four neurons**.** Single APs in L5BC (cell 1) and L5Pyr (cell 2) evoked uIPSPs and uEPSPs in L5Pyr and HEC (cell 3), respectively; APs in either of two HECs (cell 3 or 4) evoked uIPSPs in another HEC; APs in HEC (cell 3) also evoked uIPSPs in L5Pyr, but not in L5BC. (**D**) Connections between two L5BCs, L5Pyrs and L5MC. Left: five simultaneously recorded L5 neurons including two L5BCs, two L5Pyrs and one L5MC. The morphology of each neuron was spatially separated (Right). Middle: connection diagram of five neurons. Single APs elicited in L5MC evoked uIPSPs in two L5Pyrs and one L5BC, but not in another L5BC (cell 5); APs elicited in one L5BC (cell 4) evoked uIPSPs in two L5Pyrs and L5MC, but not in another L5BC (cell 5); APs elicited in cell 5 (L5BC) evoked uIPSPs only in cell 4 (another L5BC), not in other neurons. Repetitive APs elicited in one L5Pyr (cell 3) at 10Hz evoked successive uEPSPs in L5BC (cell 5), not in other neurons, and uEPSPs in L5BC were modestly depressing.

Fig. S6

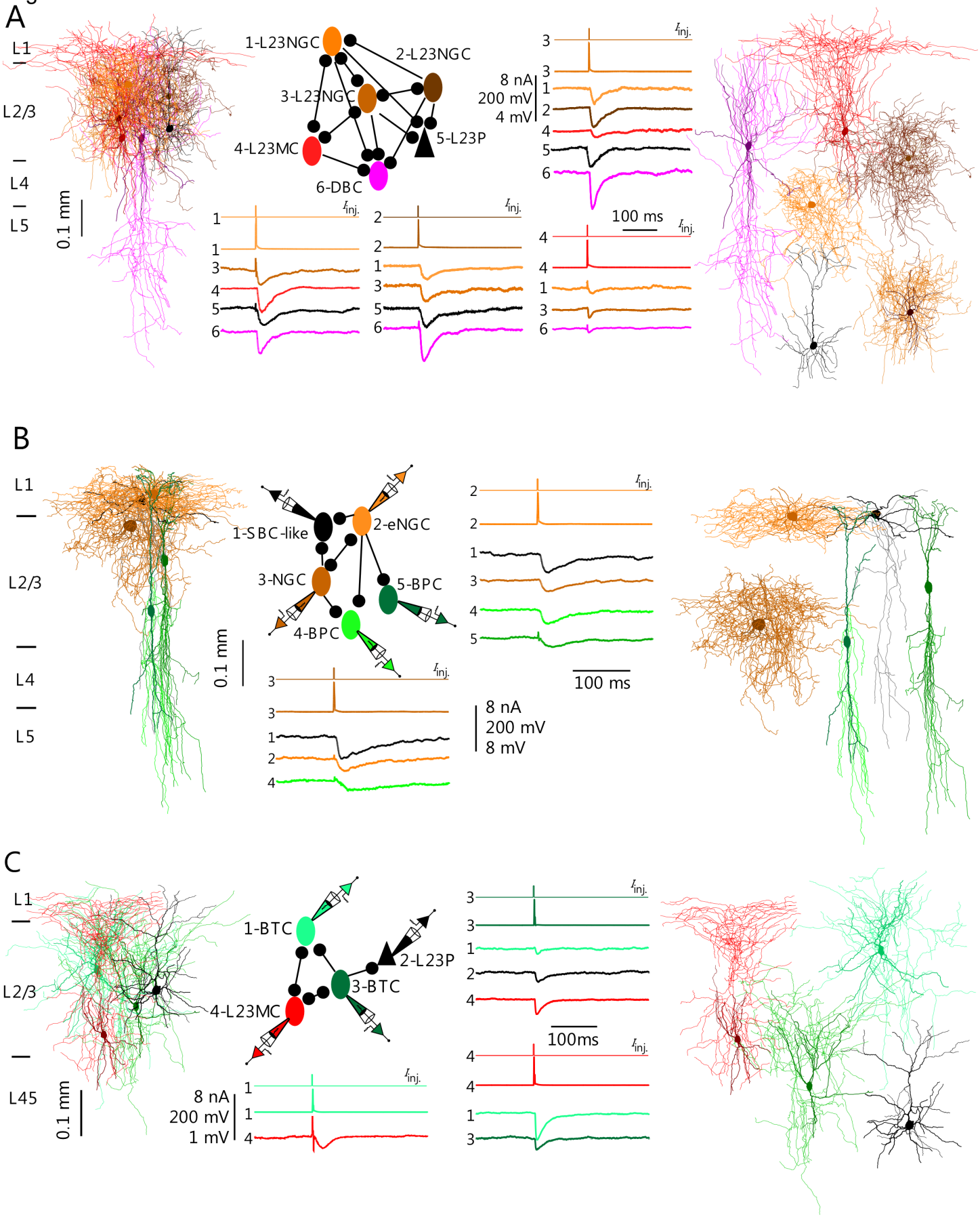
A
L1
L2/3
L4
L5
0.1 mm
1-L23NGC
2-L23NGC
3-L23NGC
4-L23MC
5-L23P
6-DBC
8 nA
200 mV
4 mV
100 ms
B
L1
L2/3
L4
L5
0.1 mm
1-SBC-like
2-eNGC
3-NGC
4-BPC
5-BPC
100 ms
8 nA
200 mV
8 mV
C
L1
L2/3
L45
0.1 mm
1-BTC
2-L23P
3-BTC
4-L23MC
100ms
8 nA
200 mV
1 mV

Fig.S6. L23NGCs projected to every type of neurons in L1 and L23, and BTC projected to L23MC and other BTCs. Vertical scale bars not showing distance show, from top to bottom, amplitudes of current injection (I_{inj} in nA), APs (mV), uIPSPs (mV). (**A**) NGCs inhibited every neuron nearby and were inhibited by L23MC. Left: six simultaneously recorded neurons including three L23NGCs, one L23MC, one DBC and one L23Pyr. The morphology of each neuron was spatially separated (Right). Middle: connection diagram of six neurons. Single APs elicited in one L23NGC (cell 1) evoked uIPSPs in all other neurons except cell 2 (NGC); APs elicited in one L23NGC (cell 2) evoked uIPSPs in all other neurons except L23MC; APs elicited in one L23NGC (cell 3) evoked uIPSPs in all other neurons; APs elicited in L23MC evoked uIPSPs in two NGCs (cell 1 and cell 3) and DBC, but not in L23Pyr and another L23NGC (cell 2). (**B**) NGCs inhibited neurons in both L1 and L23. Left: five simultaneously recorded neurons including two BPCs, one L23NGC, one eNGC and one SBC-like cell. The morphology of each neuron was spatially separated (Right). Middle: connection diagram of five neurons. Single APs elicited in eNGC evoked uIPSPs in all other neurons; APs in L23NGC evoked uIPSPs in all other neurons except one BPC (cell 5). (**C**) BTC projected to L23MC and other BTCs. Left: four simultaneously recorded neurons including two BTCs, one L23MC and one L23Pyr. The morphology of each neuron was spatially separated (Right). Middle: connection diagram of five neurons. Single APs elicited in one BTC (cell 1) evoked uIPSPs only in L23MC; APs elicited in another BTC (cell 3) evoked uIPSPs in all other neurons; APs elicited in L23MC evoked uIPSPs in both L23BTCs, but not in L23Pyr.

Fig.S7

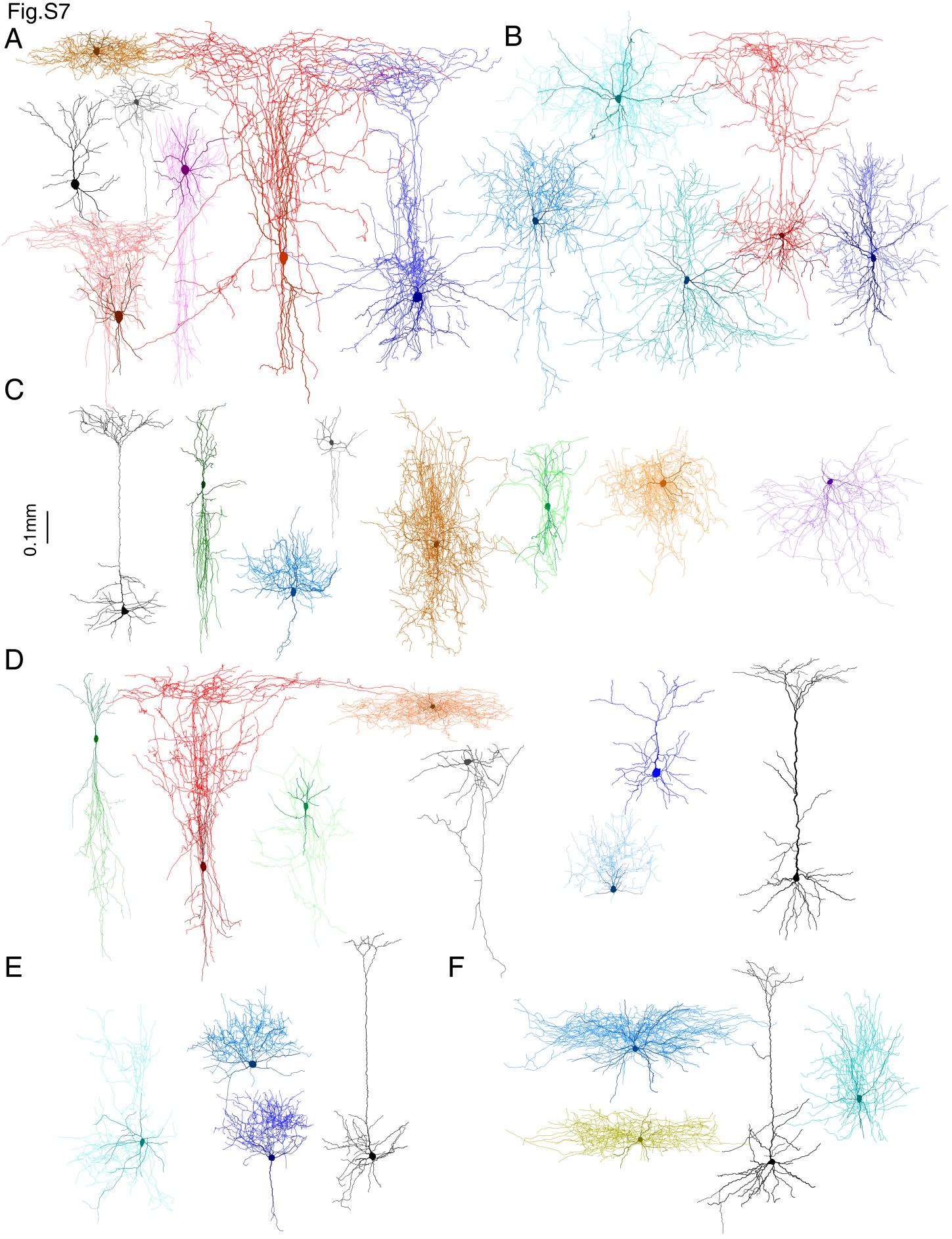

Fig.S7. The neurons in Fig.3 and Fig.S5 were spatially separated. (**A**) Spatially separated neurons from Fig.3A. (**B**) Spatially separated neurons from Fig.3B. (**C**) Spatially separated neurons from Fig.3C. (**D**) Spatially separated neurons from Fig.S5A. (**E**) Spatially separated neurons from Fig.5B. (**F**) Spatially separated neurons from Fig.5C.

Fig. S8

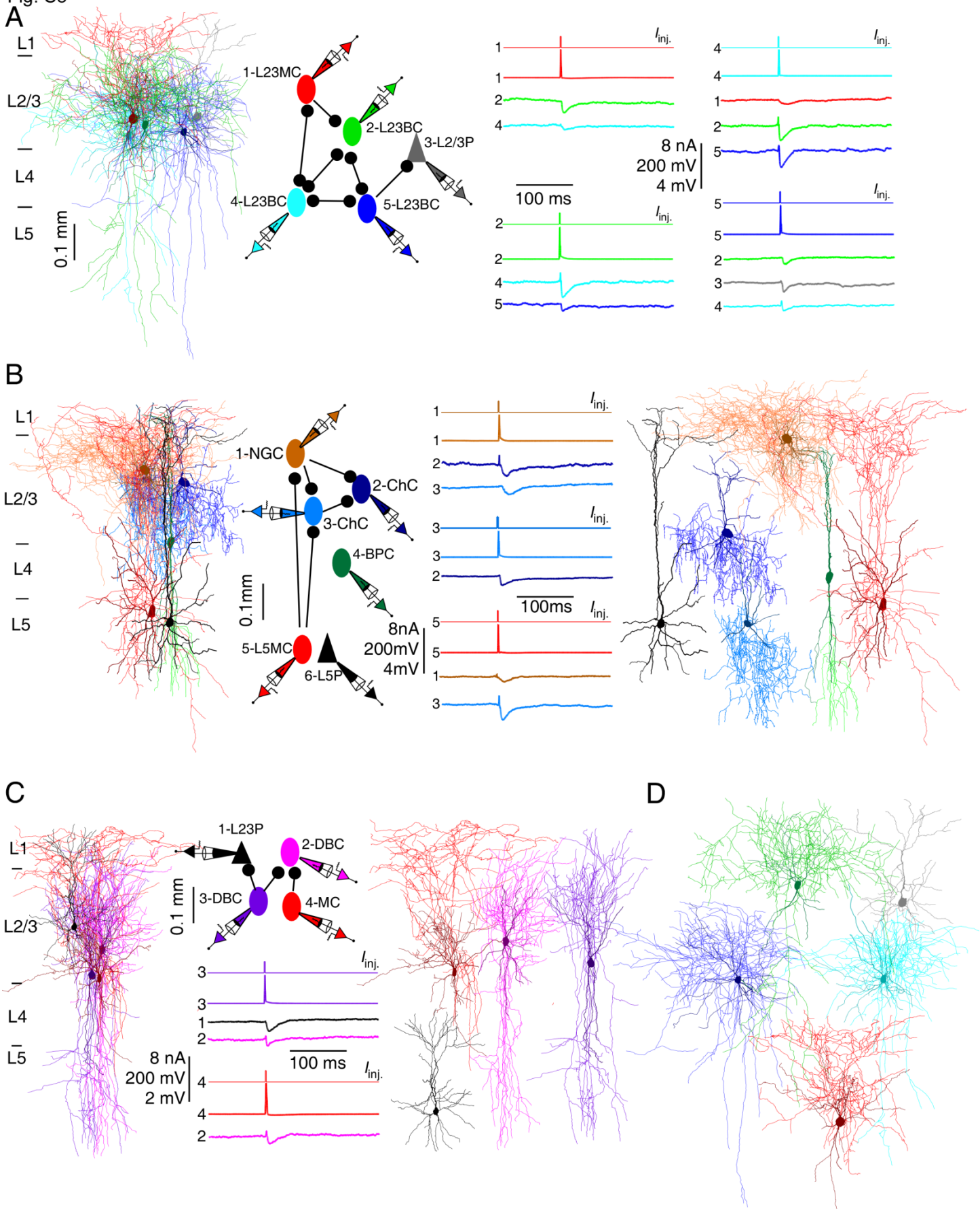
A
L1
L2/3
L4
L5
0.1 mm
1-L23MC
2-L23BC
3-L2/3P
4-L23BC
5-L23BC
$I_{inj.}$
8 nA
200 mV
4 mV
100 ms
B
L1
L2/3
L4
L5
1-NGC
2-ChC
3-ChC
4-BPC
5-L5MC
6-L5P
0.1mm
8nA
200mV
4mV
100ms
C
L1
L2/3
L4
L5
1-L23P
2-DBC
3-DBC
4-MC
0.1 mm
8 nA
200 mV
2 mV
100 ms
D

Fig.S8. Connection patterns between morphologically distinct typees of GABAergic interneurons. Vertical scale bars not showing distance show, from top to bottom, amplitudes of current injection (I_{inj} in nA), APs (mV), uIPSPs (mV). (**A**) L23BCs inhibited each other, and L23BCs mutually connected with L23MCs. Left: five simultaneously recorded, morphologically reconstructed neurons including one L23MC, one L23Pyr, three L23BCs. They were spatially separated as shown in (**D**). Middle: connection diagram of five neurons. Right: single APs elicited in L23MC (cell 1) evoked uIPSPs in two L23BCs (cell 2 and cell 4), but not in L23Pyr and other L23BC (cell 5); APs elicited in L23BC (cell 2) evoked uIPSPs in two other L23BCs, but not in L23Pyr and L23MC; APs elicited in L23BC (cell 4) evoked uIPSPs in two other L23BCs and L23MC, but not in L23Pyr; APs elicited in L23BC (cell 5) evoked uIPSPs in two other L23BCs and L23Pyr, but not in L23MC. The uIPSPs from connections between cell 2 and cell 4 were mixed with the preceding spikelets, which were confirmed to result from electrical connections. (**B**) ChCs inhibited each other and receive inhibitory inputs from L5MC and L23NGC. Left: six simultaneously recorded, morphologically reconstructed neurons including one L5MC, one L23NGC, one BPC, two ChCs and one L5Pyr, and they were spatially separated (Right). Middle: connection diagram of six neurons. Single APs elicited in L23NGC (cell 1) evoked uIPSPs in two ChCs, but not in other neurons; APs elicited in one ChC (cell 3) evoked uIPSPs in another ChC, not in other neurons; APs elicited in L5MC evoked uIPSPs in L23NGC and one ChC (cell 3), but not in other neurons. (**C**) DBCs inhibited each other and received inhibitory inputs from MC. Left: four simultaneously recorded, morphologically reconstructed neurons including one L23MC, two DBCs and one L23Pyr, and they were spatially separated (Right). Middle: connection diagram of six neurons. Single APs elicited in DBC (cell 3) evoked uIPSPs in another DBC and L23Pyr, but not in L23MC; APs elicited in L23MC evoked uIPSPs only in one DBC, not in another DBC and L23Pyr.

Fig. S9

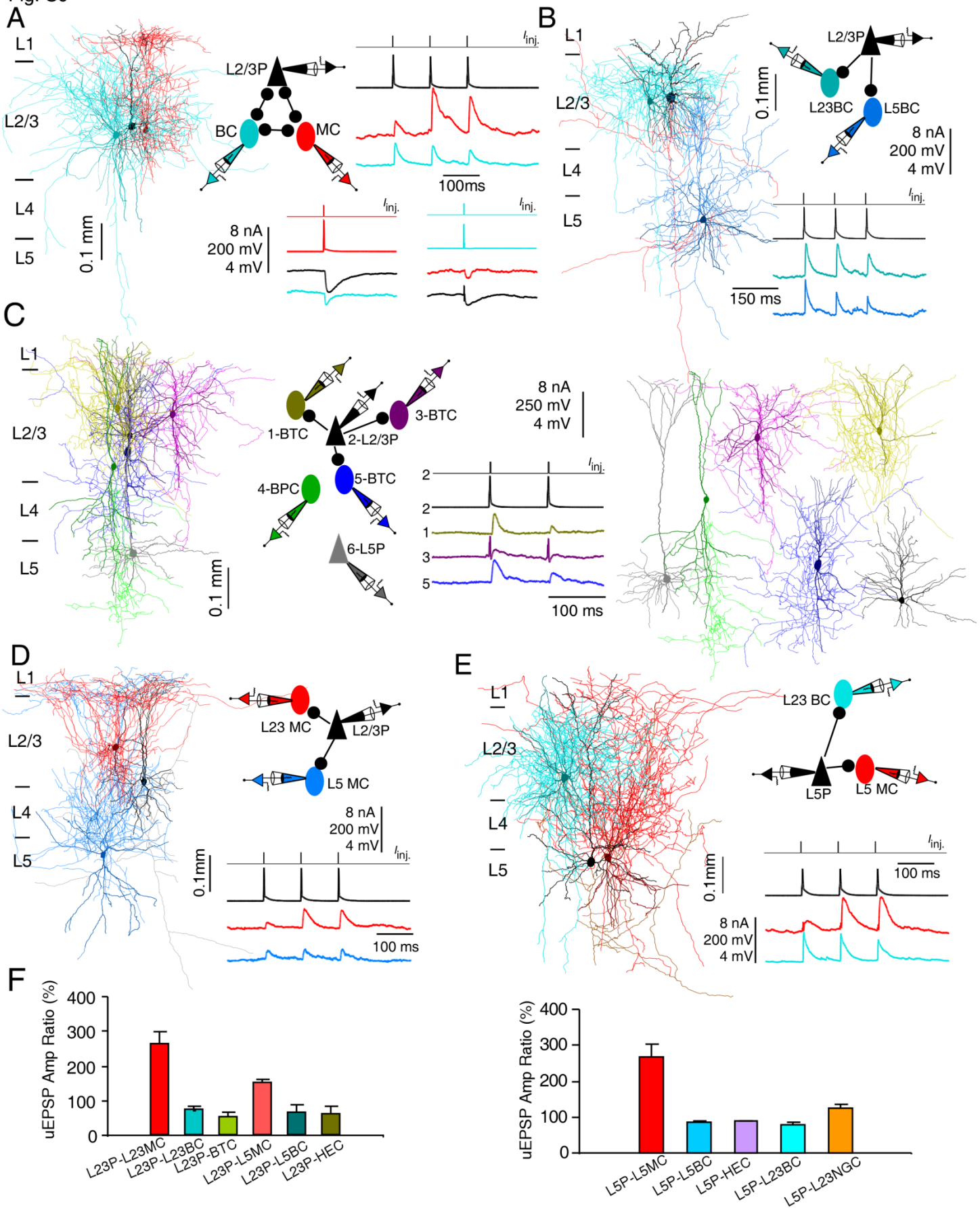
A
L1
L2/3
L4
L5
0.1 mm
L2/3P
BC
MC
$I_{inj.}$
100ms
8 nA
200 mV
4 mV
B
L1
L2/3
L4
L5
L2/3P
L23BC
L5BC
0.1mm
8 nA
200 mV
4 mV
$I_{inj.}$
150 ms
C
L1
L2/3
L4
L5
0.1 mm
1-BTC
2-L2/3P
3-BTC
4-BPC
5-BTC
6-L5P
8 nA
250 mV
4 mV
$I_{inj.}$
100 ms
D
L1
L2/3
L4
L5
L23 MC
L2/3P
L5 MC
0.1mm
8 nA
200 mV
4 mV
$I_{inj.}$
100 ms
E
L1
L2/3
L4
L5
L23 BC
L5P
L5 MC
0.1mm
$I_{inj.}$
100 ms
8 nA
200 mV
4 mV
F
uEPSP Amp Ratio (%)
400
300
200
100
0
L23P-L23MC
L23P-L23BC
L23P-BTC
L23P-L5MC
L23P-L5BC
L23P-HEC
uEPSP Amp Ratio (%)
400
300
200
100
0
L5P-L5MC
L5P-L5BC
L5P-HEC
L5P-L23BC
L5P-L23NGC

Fig.S9. Connections from pyramidal neurons to GABAergic interneurons. Vertical scale bars not showing distance show, from top to bottom, amplitudes of current injection (I_{inj} in nA), APs (mV), uIPSPs (mV). (**A**) Left: three simultaneously recorded neurons including one L23MC, one L23BC and one L23Pyr (axons of L23Pyr were omitted). Right: connection diagram of three neurons. Single APs elicited in L23BC evoked uIPSPs in other two neurons; APs elicited in L23MC evoked uIPSPs in other two neurons; repetitive APs elicited in L23Pyr at 10Hz evoked successive uEPSPs in both L23BC and L23MC, with uEPSPs in L23MC strongly facilitating and uEPSPs in L23BC weakly depressing. (**B**) Left: three simultaneously recorded neurons including one L23Pyr, one L23BC and one L5BC. Right: connection diagram of three neurons. Repetitive APs elicited in L23Pyr at 10Hz evoked successive uEPSPs in both L23BC and L5BC, and uEPSPs in both L23BC and L5BC were depressing. (**C**) Connections between six simultaneously recorded, morphologically reconstructed neurons including three BTCs, one BPC, one L23P and one L5P (Left). Each neuron was spatially separated (Right). Middle: connection diagram of six neurons**.** Repetitive APs elicited in L23P (cell 2) at 10 Hz evoked successive uIPSPs in three BTCs, not in other neurons. (**D**) Left: three simultaneously recorded neurons including one L23Pyr, one L23MC and one L5MC. Right: connection diagram of three neurons. Repetitive APs elicited in L23Pyr at 10Hz evoked successive uEPSPs in both L23MC and L5MC, with uEPSPs in L23MC strongly facilitating and uEPSPs in L5MC weakly facilitating. (**E**) Left: three simultaneously recorded neurons including one L23BC, one L5Pyr and one L5MC. Right: connection diagram of three neurons. Repetitive APs elicited in L5Pyr at 10Hz evoked successive uEPSPs in both L23BC and L5MC, with uEPSPs in L5MC strongly facilitating and uEPSPs in L23BC weakly depressing. (**F**) Pair pulse effects of uEPSPs from distinct types of interneurons.

Fig.S10

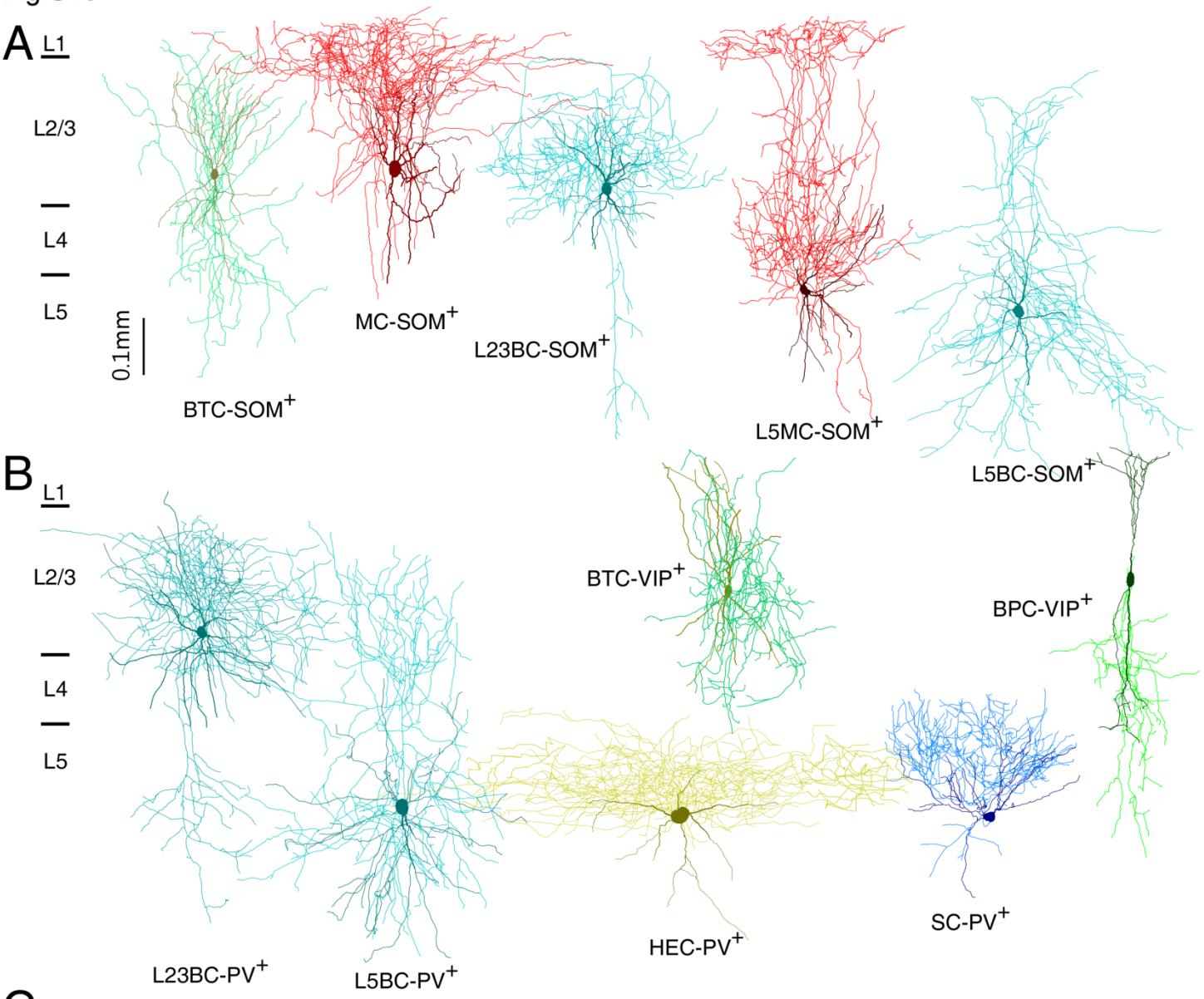
A
L1
L2/3
L4
L5
0.1mm
BTC-SOM+
MC-SOM+
L23BC-SOM+
L5MC-SOM+
L5BC-SOM+
B
L1
L2/3
L4
L5
BTC-VIP+
BPC-VIP+
L23BC-PV+
L5BC-PV+
HEC-PV+
SC-PV+

C

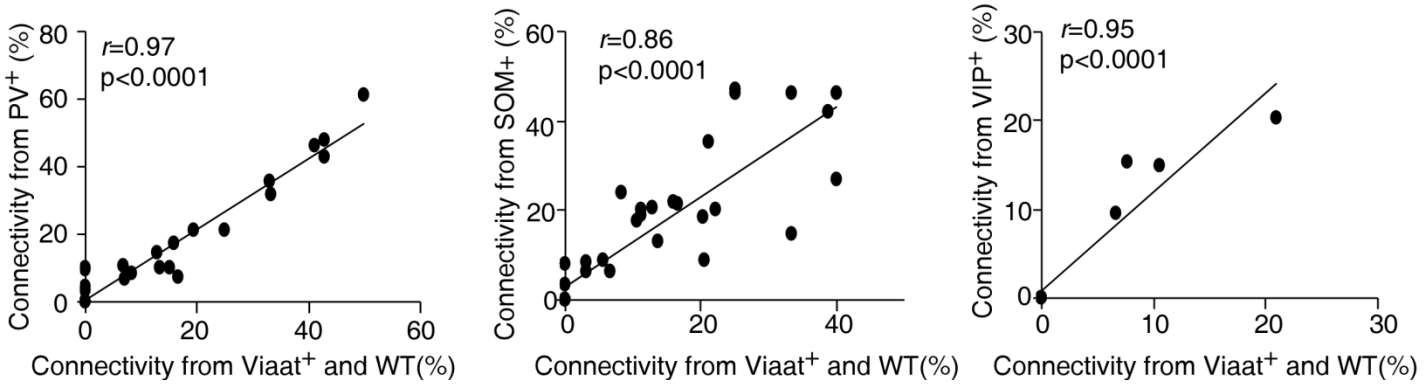
r=0.97
p<0.0001
Connectivity from PV+ (%)
Connectivity from Viaat+ and WT(%)
r=0.86
p<0.0001
Connectivity from SOM+ (%)
Connectivity from Viaat+ and WT(%)
r=0.95
p<0.0001
Connectivity from VIP+ (%)
Connectivity from Viaat+ and WT(%)

Fig.S10. The morphological diversity of interneurons from PV, SOM and VIP-Cre lines and the correlations between connectivity of labeled neurons from different Cre lines. (**A**) The morphological diversity of interneurons from SOM-Cre lines. (**B**) The morphological diversity of interneurons from PV and VIP-Cre lines. (**C**) Connectivity between distinct morphological types of PV^+ neurons and their connectivity with pyramidal neurons (Table S7) is plotted against the connectivity between corresponding morphological types from viaat/ai9 and wild-type mice. There is a strong linear relationship between connectivity from different mouse lines ($r(33)=0.97$, $p<0.0001$; left plot)). Connectivity between distinct morphological types of SOM^+ neurons and their connectivity with pyramidal neurons (Table S8) is plotted against the connectivity between corresponding morphological types from viaat/ai9 and wild-type mice. There is a strong linear relationship between connectivity from different mouse lines ($r(37)=0.86$, $p<0.0001$; middle plot). Connectivity between distinct morphological types of VIP^+ neurons and their connectivity with pyramidal neurons (Table S9) is plotted against the connectivity between corresponding morphological types from viaat/ai9 and wild-type mice. There is a strong linear relationship between connectivity from different mouse lines ($r(11)=0.95$, $p<0.0001$; right).

Fig.S11

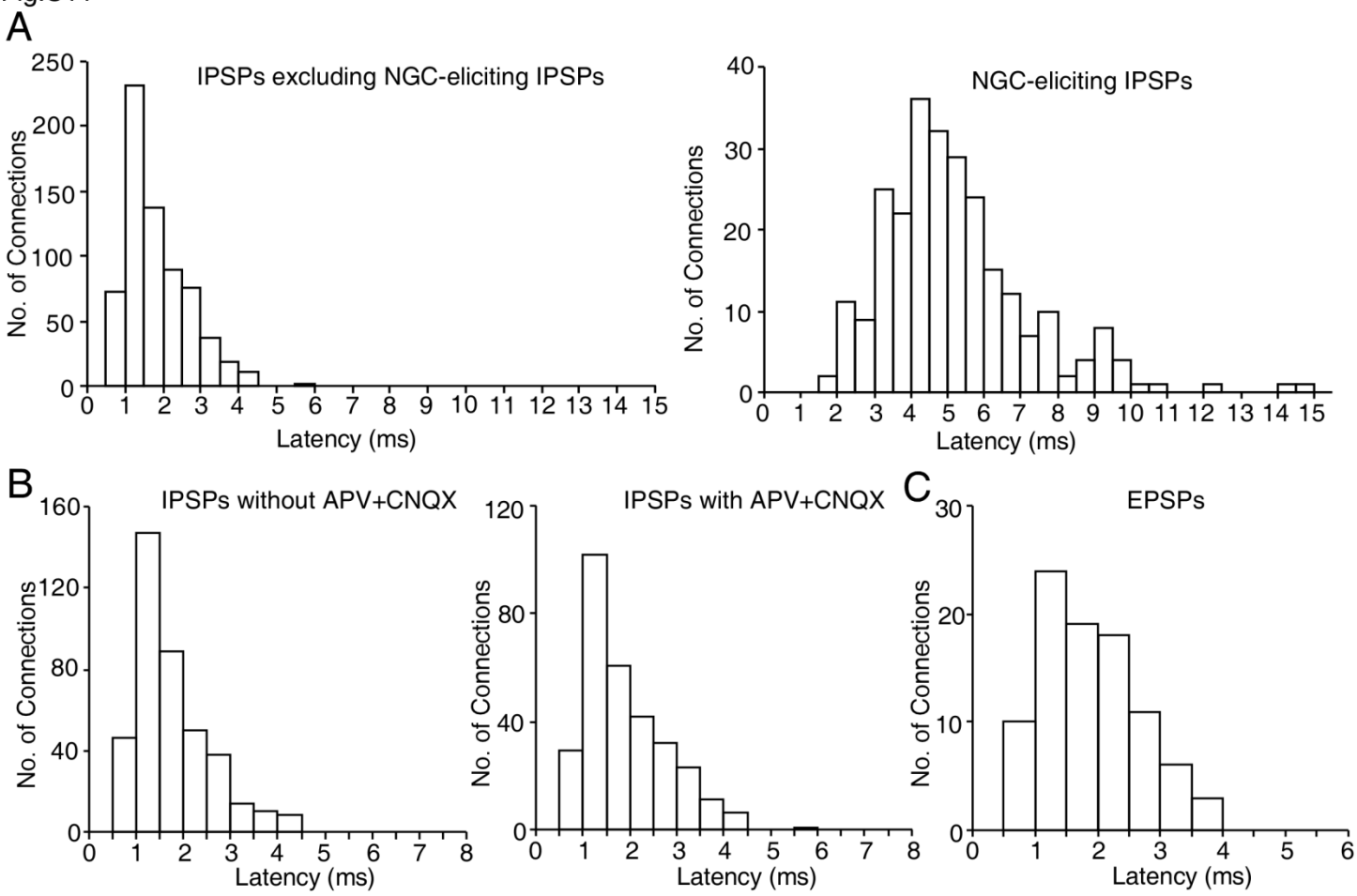

Fig. S11. The histogram of latencies of uIPSPs and uEPSPs. (**A**)The histogram of latencies of all uIPSPs except NGC-eliciting uIPSPs and the histogram of latencies of NGC-eliciting uIPSPs. (**B**) Latency comparison of uIPSPs recorded in the absence of glutaminergic antagonists (APV and CNQX) with those recorded in the presence of glutaminergic antagonists. Note the blockade of glutamatergic transmission does not shift left the distribution of latencies. (**C**) The histogram of latencies of all uEPSPs, measured from the peak of the presynaptic AP to 5% of the rise of the uEPSPs.

Fig.12

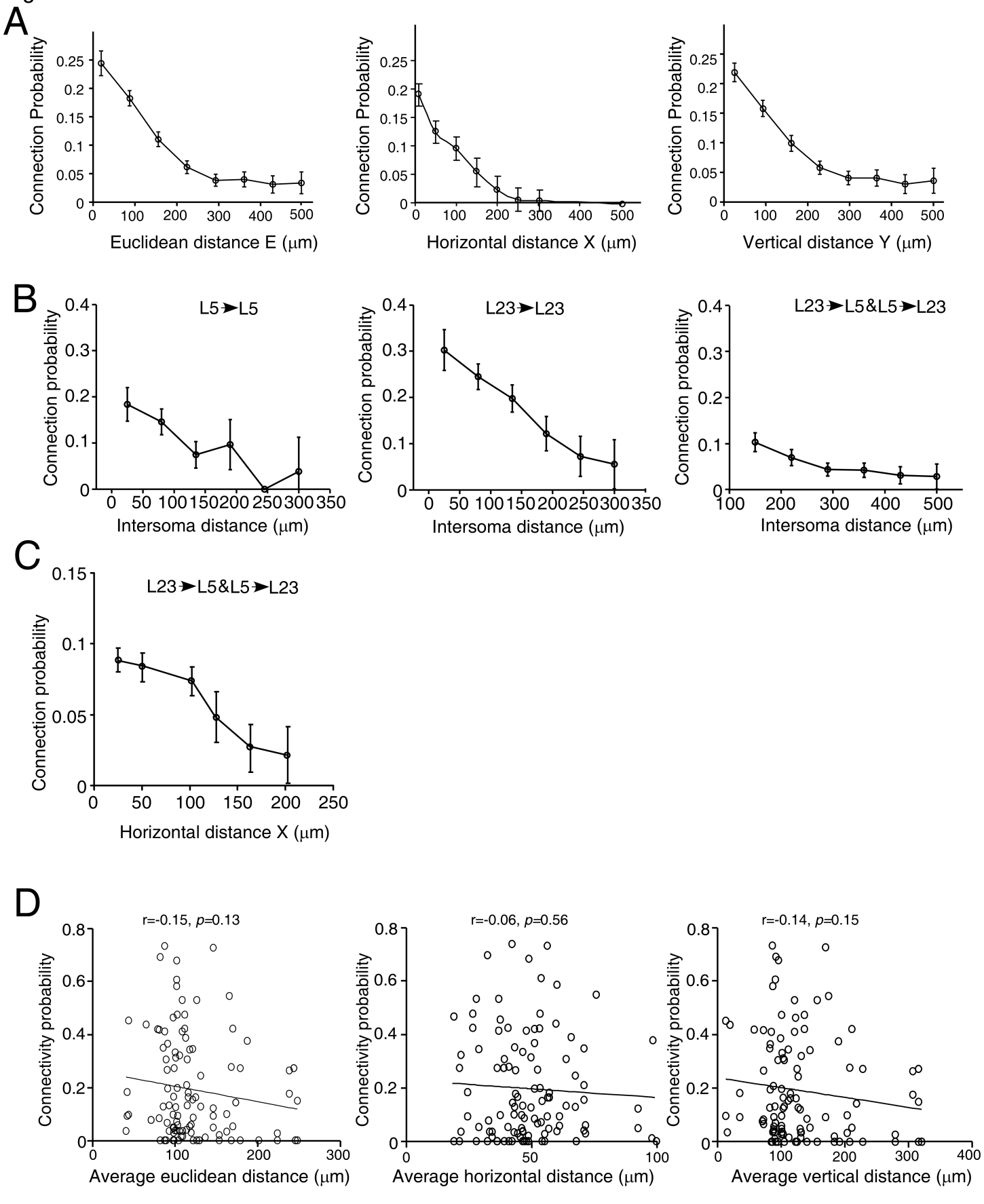
A
Connection Probability
Euclidean distance E (μm)
Horizontal distance X (μm)
Vertical distance Y (μm)
B
L5➤L5
L23➤L23
L23➤L5&L5➤L23
Connection probability
Intersoma distance (μm)
C
L23➤L5&L5➤L23
Connection probability
Horizontal distance X (μm)
D
r=-0.15, p=0.13
r=-0.06, p=0.56
r=-0.14, p=0.15
Connectivity probability
Average euclidean distance (μm)
Average horizontal distance (μm)
Average vertical distance (μm)

Fig.S12. (**A**) Connection probability profiles as a function of distance (Euclidean, horizontal and vertical). Error bars represent 95% confidence interval. (**B**) The inhibitory connectivity between L5 neurons as a function of inter-soma distance (left), the inhibitory connectivity between L23 neurons as a function of inter-soma distance (middle), and the inhibitory connectivity between L23 neurons and L5 neurons as a function of inter-soma distance (right). Note the connection probabilities within L23 are higher than within L5 in all ranges of inter-soma distance. (**C**) The inhibitory connectivity between L23 neurons and L5 neurons as a function of inter-soma horizontal distance. (**D**) Scatter plots show the connectivity of each type of connections as a function of the average Euclidean, horizontal and vertical distances between the neuronal pairs in this type of connection.

Fig.S13

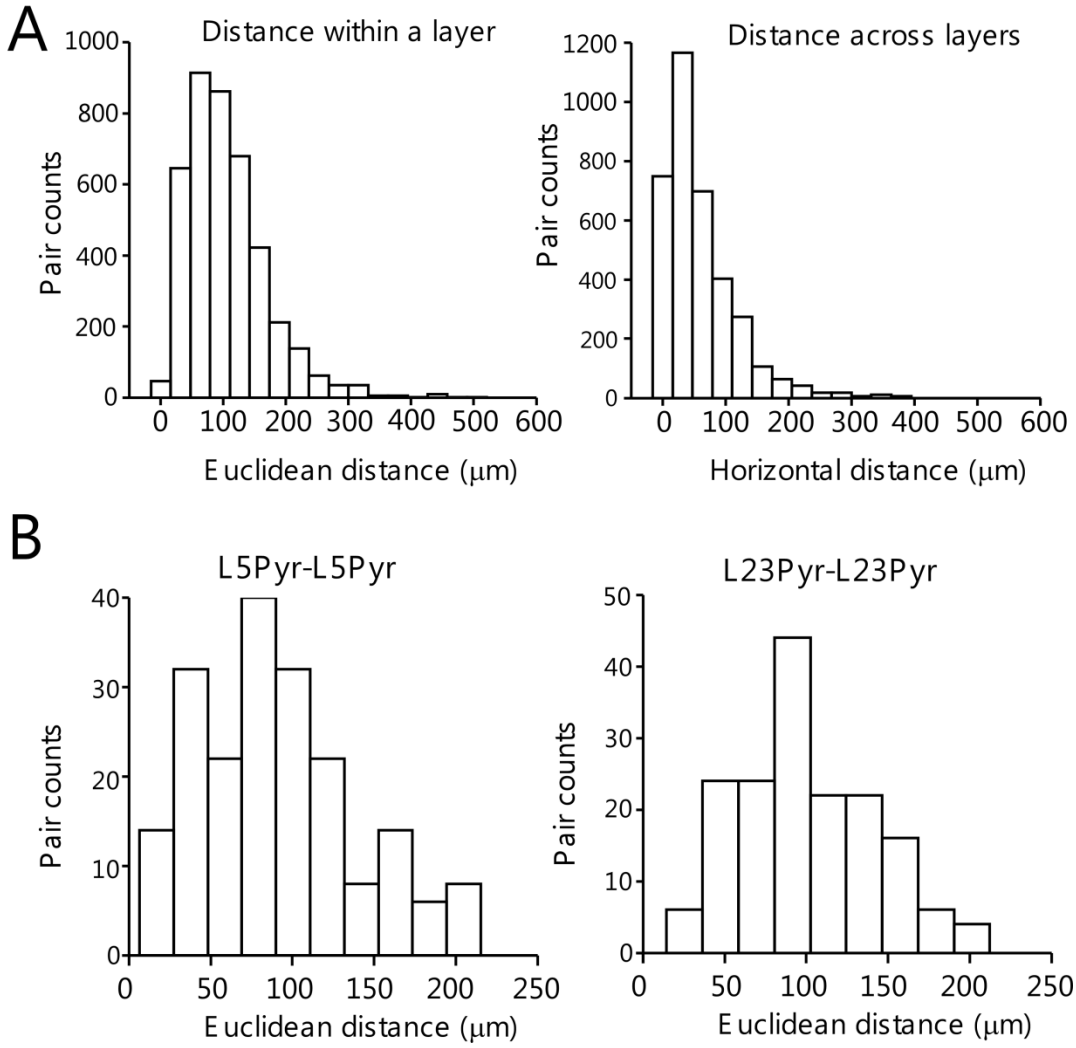

Fig. S13. (**A**)The histogram of the Euclidean distances between all recorded neurons within a layer and the histogram of the horizontal distances between all recorded neurons across layers. (**B**) The histogram of Euclidean distances between recorded L5 pyramidal neurons, and between recorded L23 pyramidal neurons.

Fig.S14

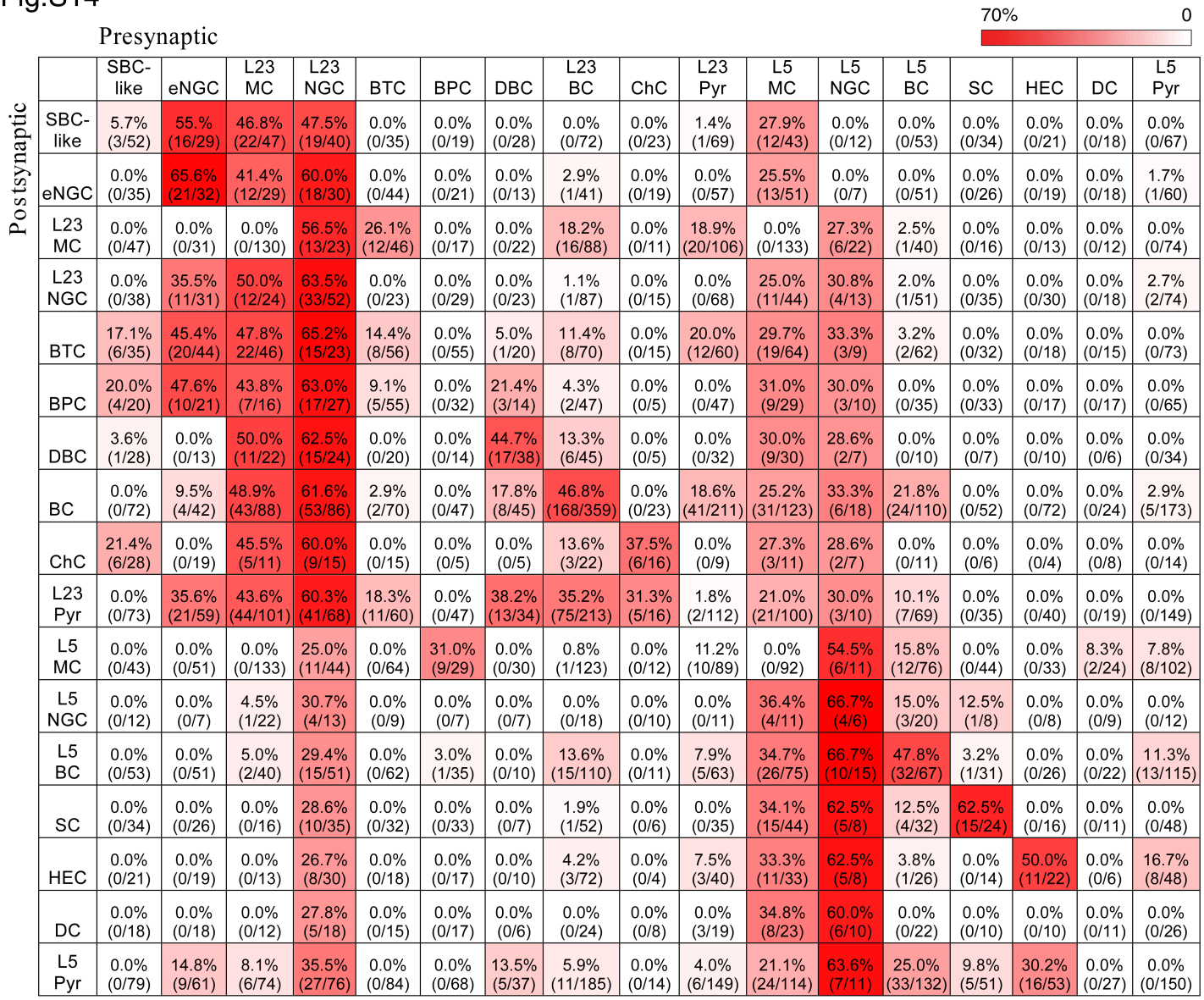

	SBC-like	eNGC	L23 MC	L23 NGC	BTC	BPC	DBC	L23 BC	ChC	L23 Pyr	L5 MC	L5 NGC	L5 BC	SC	HEC	DC	L5 Pyr
SBC-like	5.7% (3/52)	55.% (16/29)	46.8% (22/47)	47.5% (19/40)	0.0% (0/35)	0.0% (0/19)	0.0% (0/28)	0.0% (0/72)	0.0% (0/23)	1.4% (1/69)	27.9% (12/43)	0.0% (0/12)	0.0% (0/53)	0.0% (0/34)	0.0% (0/21)	0.0% (0/18)	0.0% (0/67)
eNGC	0.0% (0/35)	65.6% (21/32)	41.4% (12/29)	60.0% (18/30)	0.0% (0/44)	0.0% (0/21)	0.0% (0/13)	2.9% (1/41)	0.0% (0/19)	0.0% (0/57)	25.5% (13/51)	0.0% (0/7)	0.0% (0/51)	0.0% (0/26)	0.0% (0/19)	0.0% (0/18)	1.7% (1/60)
L23 MC	0.0% (0/47)	0.0% (0/31)	0.0% (0/130)	56.5% (13/23)	26.1% (12/46)	0.0% (0/17)	0.0% (0/22)	18.2% (16/88)	0.0% (0/11)	18.9% (20/106)	0.0% (0/133)	27.3% (6/22)	2.5% (1/40)	0.0% (0/16)	0.0% (0/13)	0.0% (0/12)	0.0% (0/74)
L23 NGC	0.0% (0/38)	35.5% (11/31)	50.0% (12/24)	63.5% (33/52)	0.0% (0/23)	0.0% (0/29)	0.0% (0/23)	1.1% (1/87)	0.0% (0/15)	0.0% (0/68)	25.0% (11/44)	30.8% (4/13)	2.0% (1/51)	0.0% (0/35)	0.0% (0/30)	0.0% (0/18)	2.7% (2/74)
BTC	17.1% (6/35)	45.4% (20/44)	47.8% 22/46)	65.2% (15/23)	14.4% (8/56)	0.0% (0/55)	5.0% (1/20)	11.4% (8/70)	0.0% (0/15)	20.0% (12/60)	29.7% (19/64)	33.3% (3/9)	3.2% (2/62)	0.0% (0/32)	0.0% (0/18)	0.0% (0/15)	0.0% (0/73)
BPC	20.0% (4/20)	47.6% (10/21)	43.8% (7/16)	63.0% (17/27)	9.1% (5/55)	0.0% (0/32)	21.4% (3/14)	4.3% (2/47)	0.0% (0/5)	0.0% (0/47)	31.0% (9/29)	30.0% (3/10)	0.0% (0/35)	0.0% (0/33)	0.0% (0/17)	0.0% (0/17)	0.0% (0/65)
DBC	3.6% (1/28)	0.0% (0/13)	50.0% (11/22)	62.5% (15/24)	0.0% (0/20)	0.0% (0/14)	44.7% (17/38)	13.3% (6/45)	0.0% (0/5)	0.0% (0/32)	30.0% (9/30)	28.6% (2/7)	0.0% (0/10)	0.0% (0/7)	0.0% (0/10)	0.0% (0/6)	0.0% (0/34)
BC	0.0% (0/72)	9.5% (4/42)	48.9% (43/88)	61.6% (53/86)	2.9% (2/70)	0.0% (0/47)	17.8% (8/45)	46.8% (168/359)	0.0% (0/23)	18.6% (41/211)	25.2% (31/123)	33.3% (6/18)	21.8% (24/110)	0.0% (0/52)	0.0% (0/72)	0.0% (0/24)	2.9% (5/173)
ChC	21.4% (6/28)	0.0% (0/19)	45.5% (5/11)	60.0% (9/15)	0.0% (0/15)	0.0% (0/5)	0.0% (0/5)	13.6% (3/22)	37.5% (6/16)	0.0% (0/9)	27.3% (3/11)	28.6% (2/7)	0.0% (0/11)	0.0% (0/6)	0.0% (0/4)	0.0% (0/8)	0.0% (0/14)
L23 Pyr	0.0% (0/73)	35.6% (21/59)	43.6% (44/101)	60.3% (41/68)	18.3% (11/60)	0.0% (0/47)	38.2% (13/34)	35.2% (75/213)	31.3% (5/16)	1.8% (2/112)	21.0% (21/100)	30.0% (3/10)	10.1% (7/69)	0.0% (0/35)	0.0% (0/40)	0.0% (0/19)	0.0% (0/149)
L5 MC	0.0% (0/43)	0.0% (0/51)	0.0% (0/133)	25.0% (11/44)	0.0% (0/64)	31.0% (9/29)	0.0% (0/30)	0.8% (1/123)	0.0% (0/12)	11.2% (10/89)	0.0% (0/92)	54.5% (6/11)	15.8% (12/76)	0.0% (0/44)	0.0% (0/33)	8.3% (2/24)	7.8% (8/102)
L5 NGC	0.0% (0/12)	0.0% (0/7)	4.5% (1/22)	30.7% (4/13)	0.0% (0/9)	0.0% (0/7)	0.0% (0/7)	0.0% (0/18)	0.0% (0/10)	0.0% (0/11)	36.4% (4/11)	66.7% (4/6)	15.0% (3/20)	12.5% (1/8)	0.0% (0/8)	0.0% (0/9)	0.0% (0/12)
L5 BC	0.0% (0/53)	0.0% (0/51)	5.0% (2/40)	29.4% (15/51)	0.0% (0/62)	3.0% (1/35)	0.0% (0/10)	13.6% (15/110)	0.0% (0/11)	7.9% (5/63)	34.7% (26/75)	66.7% (10/15)	47.8% (32/67)	3.2% (1/31)	0.0% (0/26)	0.0% (0/22)	11.3% (13/115)
SC	0.0% (0/34)	0.0% (0/26)	0.0% (0/16)	28.6% (10/35)	0.0% (0/32)	0.0% (0/33)	0.0% (0/7)	1.9% (1/52)	0.0% (0/6)	0.0% (0/35)	34.1% (15/44)	62.5% (5/8)	12.5% (4/32)	62.5% (15/24)	0.0% (0/16)	0.0% (0/11)	0.0% (0/48)
HEC	0.0% (0/21)	0.0% (0/19)	0.0% (0/13)	26.7% (8/30)	0.0% (0/18)	0.0% (0/17)	0.0% (0/10)	4.2% (3/72)	0.0% (0/4)	7.5% (3/40)	33.3% (11/33)	62.5% (5/8)	3.8% (1/26)	0.0% (0/14)	50.0% (11/22)	0.0% (0/6)	16.7% (8/48)
DC	0.0% (0/18)	0.0% (0/18)	0.0% (0/12)	27.8% (5/18)	0.0% (0/15)	0.0% (0/17)	0.0% (0/6)	0.0% (0/24)	0.0% (0/8)	0.0% (3/19)	34.8% (8/23)	60.0% (6/10)	0.0% (0/22)	0.0% (0/10)	0.0% (0/10)	0.0% (0/11)	0.0% (0/26)
L5 Pyr	0.0% (0/79)	14.8% (9/61)	8.1% (6/74)	35.5% (27/76)	0.0% (0/84)	0.0% (0/68)	13.5% (5/37)	5.9% (11/185)	0.0% (0/14)	4.0% (6/149)	21.1% (24/114)	63.6% (7/11)	25.0% (33/132)	9.8% (5/51)	30.2% (16/53)	0.0% (0/27)	0.0% (0/150)

Fig.S14 Connectivity matrix for the mouse V1. Color-coded matrix showing the probability of finding a connected pair of neurons between two specific types of neurons within and across layers, which is denoted as % (total connections found/total connections tested). The mean amplitudes of uIPSPs and uEPSPs for each type of connections are presented in Table S6.

Table S1. Intrinsic Electrophysiological Properties of GABAergic Interneurons in Mature Visual Cortex

		Resting V_m (mV)	R_{in} (MΩ)	Tau (ms)	AP threshold (mV)	AP amplitude (mV)	AP half-width (ms)	AHP (mV)	ADP %/Amp (mV)	AI (%)	Max. frequency (spike/s)	LS (% of neuron)	BS (% of neuron)
L1	eNGC	-66.7±1.4	132.8±6.0	4.3±0.1	-38.3±0.7	60.4±1.5	1.04±0.03	13.8±0.4	0.0% /0±0.0	130.7±4.7	15.7±0.7	90.0%	0.0%
	SBC-like	-69.8±1.4	136.8±5.4	5.2±0.2	-45.0±0.6	69.1±1.0	0.92±0.02	7.3±0.5	91.2%/ 3.9±0.4	518.4±140.0	15.2±1.2	3.2%	42.6%
L23	MC	-66.3±0.9	126.1±3.6	9.1±0.4	-42.4±0.9	68.6±1.9	0.80±0.02	12.8±0.5	0.0%/ 0±0.0	138.5±4.8	25.5±2.4	0.0%	0.0%
	NGC	-66.7±1.1	120.6±7.1	4.7±0.2	-37.2±1.3	63.6±2.8	0.94.6±0.04	11.5±0.7	7.7%/ 2.1±0.3	190.3±15.6	20.0±2.1	98.2%	0.0%
	BTC	-66.5±1.3	131.6±5.6	5.8±0.5	-44.2±1.0	79.7±1.6	0.75±0.02	9.6±0.9	53.6%/ 5.0±0.5	235.5±11.8	19.1±2.0	0.0%	13.3%
	BPC	-77.4±1.6	131.2±5.4	4.2±0.3	-46.4±1.4	84.6±1.5	0.78.6±0.03	7.8±1.1	90.4%/ 5.4±0.9	380.5±35.2	13.2±1.6	0.0%	40.0%
	BC	-68.1±1.1	84.5±3.9	3.9±0.2	-44.1±1.0	62.2±1.0	0.66±0.01	18.2±0.4	0.0%/ 0±0.0	109.0±1.3	145.2±2.8	0.0%	0.0%
	DBC	-67.6±1.3	76.7±2.7	4.6±0.2	-41.9±1.1	61.0±1.5	0.62±0.02	19.7±0.4	0.0%/ 0±0.0	111.4±1.9	152.8±4.8	0.0%	0.0%
	ChC	-71.3±1.4	111.7±5.8	4.4±0.4	-43.8±1.6	60.2±3.2	0.59±0.02	18.8±0.8	0.0%/ 0±0.0	108.5±4.2	150.0±6.7	0.0%	0.0%
L5	MC	-66.6±1.1	141.8±7.1	9.1±0.4	-48.2±0.7	70.2±0.9	0.83±0.02	11.7±0.4	0.0%/ 0±0.0	164.8±10.2	13.4±1.1	0.0%	0.0%
	NGC	-63.3±1.8	95.4±6.4	5.3±0.2	-35.2±1.7	59.2±3.3	0.94±0.04	13.5±1.1	7.5/ 2.1±0.5	197.7±20.8	20.5±2.7	100.0%	0.0%
	BC	-68.0±1.0	95.8±4.0	4.9±0.2	-47.1±0.7	56.5±0.9	0.70±0.01	18.5±0.4	0.0%/ 0±0.0	108.6±1.1	142.6±4.8	0.0%	0.0%
	SC	-66.5±1.0	105.0±5.1	4.9±0.2	-47.5±0.8	59.7±1.3	0.71±0.01	18.8±0.7	0.0%/ 0±0.0	109.3±1.8	142.8±4.1	0.0%	0.0%
	HEC	-66.8±1.1	111.5±4.9	4.9±0.2	-46.8±1.1	59.7±1.6	0.73±0.02	17.9±0.8	0.0%/ 0±0.0	113.6±6.5	138.8±5.8	0.0%	0.0%
	DC	-70.6±2.3	141.5±15.6	5.3±0.5	-49.6±2.4	75.7±3.0	0.85±0.03	9.5±1.7	30.0%/ 4.9±0.9	276.0±65.3	25.7±6.9	0.0%	25.0%

Table S1. Intrinsic electrophysiological properties of GABAergic interneurons in mature visual cortex. R_{in} denotes the input resistance. Tau denotes membrane time constant. AHP denotes the afterhyperpolarization. ADP (%/Amp) denotes the percentage of neurons with afterdepolarization following action potentials (APs) and the ADP amplitude (mV). AI denotes the firing adaptation index. Max. frequency denotes the maximum firing frequency. LS denotes late-spiking firing pattern, and the percentages of neurons with LS in each type of interneurons were calculated. BS denotes the burst-spiking firing pattern, and the percentages of neurons with BS were calculated. Values are mean ± SEM. Statistically significant differences ($p < 0.05$) were assessed by performing a nonparametric Kruskal-Wallis test followed by a post hoc Dunn-Holland-Wolfe test for pairwise comparison. Statistically significant differences between layer 1 neurons were found for the following: eNGC versus SBC-Like in AP threshold, AP amplitude, AHP and AI. Statistically significant differences between layers 2/3 interneurons were found for the following: Resting Vm: BPC versus L23MC, BPC versus L23NGC, BPC versus BTC, BPC versus DBC, BPC versus L23BC, BPC versus ChC. Rin: DBC versus L23MC, DBC versus L23NGC, DBC versus L23BTC, DBC versus BPC, DBC versus ChC, L23BC versus L23MC, L23BC versus L23NGC, L23BC versus L23BTC, L23BC versus BPC. Tau: L23MC versus L23NGC, L23MC versus BTC, L23MC versus BPC, L23MC versus DBC, L23MC versus L23BC, L23MC versus ChC, L23BC versus BTC. AP threshold: L23NGC versus L23MC, L23NGC versus BPC, L23NGC versus BTC, L23NGC versus DBC, L23NGC versus L23BC, L23NGC versus ChC. AP amplitude: BPC versus L23MC, BPC versus L23NGC, BPC versus DBC, BPC versus L23BC, BPC versus ChC, BTC versus L23MC, BTC versus L23

NGC, and BTC versus DBC, BTC versus L23BC, BTC versus ChC. AP half-width: DBC versus L23MC, DBC versus L23NGC, DBC versus BTC, DBC versus BPC, L23NGC versus L23MC, L23NGC versus BTC, L23NGC versus BPC, L23NGC versus DBC, L23NGC versus L23BC, L23NGC versus ChC, L23MC versus L23BC, L23MC versus ChC. AHP: BPC versus L23MC, BPC versus DBC, BPC versus L23BC, BPC versus ChC, BTC versus DBC, BTC versus L23BC, BTC versus ChC, L23MC versus DBC, L23MC versus L23BC, L23MC versus ChC. L23NGC versus DBC, L23NGC versus L23BC, L23NGC versus ChC. AI: L23BC versus L23MC, L23BC versus L23NGC, L23BC versus BTC, L23BC versus BPC, ChC versus L23MC, ChC versus L23NGC, ChC versus BTC, ChC versus BPC, DBC versus L23MC, DBC versus L23NGC, DBC versus BTC, DBC versus BPC, L23MC versus BPC. Max Frequency: L23BC versus L23MC, L23BC versus L23NGC, L23BC versus BTC, L23BC versus BPC, ChC versus L23MC, ChC versus L23NGC, ChC versus BTC, ChC versus BPC, DBC versus L23MC, DBC versus L23NGC, DBC versus BTC, DBC versus BPC. Statistically significant differences between layers 5 interneurons were found for the following: Rin: L5BC versus L5MC, L5BC versus DC. Tau: L5MC versus L5NGC, L5MC versus SC, L5MC versus L5BC, L5MC versus HEC, L5MC versus DC. AP threshold: L5NGC versus L5MC, L5NGC versus SC, L5NGC versus L5BC, L5NGC versus HEC, L5NGC versus DC. AP amplitude: L5MC versus L5NGC, L5MC versus SC, L5MC versus L5BC, L5MC versus HEC, DC versus L5NGC, DC versus SC, DC versus L5BC, DC versus HEC. AP half-width: L5BC versus L5MC, L5BC versus L5NGC, L5BC versus DC, L5NGC versus L5MC, L5NGC versus HEC, L5NGC versus SC, L5NGC versus DC. AHP: DC versus L5BC, DC versus SC, DC versus HEC, L5MC versus L5BC, L5MC versus SC, L5MC versus HEC, L5NGC versus L5BC, L5NGC versus SC, L5NGC versus HEC. AI: DC versus L5BC, DC versus SC, DC versus HEC, L5MC versus L5BC, L5MC versus SC, L5MC versus HEC, L5NGC versus L5BC, L5NGC versus SC, L5NGC versus HEC. Max Frequency: DC versus L5BC, DC versus SC, DC versus HEC, L5MC versus L5BC, L5MC versus SC, L5MC versus HEC, L5NGC versus L5BC, L5NGC versus SC, L5NGC versus HEC.

Table S2. Intrinsic Electrophysiological Properties of Classic SBCs and Atypical SBCs

	Resting V_m (mV)	R_{in} (MΩ)	Tau (ms)	AP threshold (mV)	AP amplitude (mV)	AP half-width (ms)	AHP (mV)	ADP %/Amp (mV)	AI (%)	Max. frequency (spike/s)	LS (% of neuron)	BS (% of neuron)
Classic SBC	-70.1±2.3	136.8±8.4	5.1±0.3	-46.0±0.9	68.1±1.4	0.91±0.03	7.9±0.8	90.0% /4.2±0.6	385±99	13.8±1.2	2.1%	35.6%
Atypical SBC	-68.6±4.9	132.8±9.6	5.2±0.5	-43.8±2.5	67.6±3.7	0.95±0.07	7.4±0.7	100%/ 4.2±0.6	480±163	13.0±2.2	4.2%	44.2%

Table S2. Intrinsic electrophysiological properties of classic SBCs and atypical SBCs. Statistically significant differences ($p < 0.05$) were assessed by performing Mann-Whitney rank sum nonparametric test. Statistically significant differences between two groups of SBC-like cells were not found for any electrophysiological parameter.

Table S3. Projections from Classic SBCs and Atypical SBCs to L23 neurons		
pre-synaptic	Postsynaptic	
	L23 interneurons	L23 pyramidal neurons
Classic SBC	7.3% (8/109)	% (0/36)
Atypical SBC	6.5% (8/123)	% (0/35)

Table S3. Projections from classic SBCs and atypical SBCs to L23 neurons

Table S4. Morphology of Labeled Neurons from Four Mouse Cre Lines																		
Cre lines \ Cell types		eNGC	SBC-like	L23 MC	L23 NGC	BTC	BPC	DBC	L23 BC	ChC	L23 Pyr	L5 MC	L5 NGC	L5 BC	SC	HEC	DC	L5 Pyr
Viaat	L1 (n=31)	17 (55%)	14 (45%)	---	---	---	---	---	---	---	---	---	---	---	---	---	---	---
	L23 (n=402)	---	---	44 (11%)	56 (14%)	69 (17%)	40 (10%)	25 (6%)	159 (39%	8 (2%)	1 (0.3%)	---	---	---	---	---	---	---
	L5 (n=289)	---	---	---	---	---	---	---	---	---	---	87 (30%)	7 (2.5%)	87 (30%)	49 (17%)	26 (9%)	13 (4.5%)	20 (7%)
PV	L23 (n=82)	---	---	0 (0%)	0 (0%)	0 (0%)	0 (0%)	0 (0%)	80 (97.5%)	2 (2.5%)	0 (0%)							
	L5 (n=43)	---	---	---	---	---	---	---	---	---	---	0 (0%)	0 (0%)	26 (60%)	10 (23%)	8 (19%)	0 (0%)	0 (0%)
SOM	L23 (n=100)	---	---	66 (66%)	0 (0%)	10 (10%)	0 (0%)	0 (0%)	24 (24%)	0 (0%)	0 (0%)	---	---	---	---	---	---	---
	L5 (n=90)	---	---	---	---	---	---	---	---	---	---	67 (74%)	0 (0%)	17 (19%)	0 (0%)	1 (1.1%)	1 (1.1%)	0 (0%)
VIP	L23 (n=40)	---	---	0 (0%)	0 (0%)	20 (55%)	18 (45%)	0 (0%)	0 (0%)	0 (0%)	0 (0%)	---	---	---	---	---	---	---
	L5 (n=2)	---	---	---	---	---	---	---	---	---	---	0 (0%)	0 (0%)	0 (0%)	0 (0%)	0 (0%)	0 (0%)	0 (0%)

Table S4. Morphology of labeled neurons from four mouse Cre lines.

Table S5. Nomenclature of morphologically identified cell types

Abbreviation	Name	Layer	Genetic Marker
eNGC	Elongated Neurogliaform Cell	L1	
SBC-like	Single-bouquet Cell-like Cell	L1	
MC	Martinotti Cell	L23, L5	SOM
NGC	Neurogliaform Cell	L23, L5	
BTC	Bitufted Cell	L23	VIP, SOM
BPC	Bipolar Cell	L23	VIP
DBC	Double Bouquet Cell	L23	
BC	Basket Cell	L23,L5	PV, SOM
ChC	Chandelier Cell	L23	PV
SC	Shrub Cell	L5	PV
HEC	Horizontally-Elongated Cell	L5	PV
DC	Deep-Projecting Cell	L5	

Table S5. Nomenclature of morphologically identified cell types and their genetic markers.

Table S6. Amplitude of uIPSPs and uEPSPs from Different Types of Connections (mV)																	
Post-synaptic	Presynaptic																
	SBC-like	eNGC	L23 MC	L23 NGC	BTC	BPC	DBC	L23 BC	ChC	L23 Pyr	L5 MC	L5 NGC	L5 BC	SC	HEC	DC	L5 Pyr
SBC-like	0.47± 0.15	1.80± 0.49	0.50± 0.09	0.75± 0.12	----	----	----	----	----	0.18	0.35± 0.11	----	----	----	----	----	----
eNGC	----	1.73± 0.55	0.50± 0.11	1.03± 0.22	----	----	----	0.37	----	----	0.31± 0.07	----	----	----	----	----	0.76
L23MC	----	----	0.15	0.75± 0.11	0.32± 0.05	----	----	0.42± 0.10	----	0.86± 0.15	----	0.75± 0.39	0.19	----	----	----	----
L23NGC	----	0.78± 0.18	0.45± 0.11	0.84± 0.13	----	----	----	----	----	----	0.22± 0.04	0.31± 0.10	0.37	----	----	----	0.93± 0.57
BTC	0.47± 0.19	0.78± 0.10	0.46± 0.10	1.36± 0.35	0.44± 0.08	----	0.10	0.41± 0.08	----	1.31± 0.32	0.70± 0.24	0.52± 0.16	0.33± 0.19	----	----	----	----
BPC	0.62± 0.19	1.10± 0.24	0.58± 0.27	0.86± 0.14	0.30± 0.10	----	0.52± 0.21	0.41± 0.05	----	----	0.42± 0.10	0.64± 0.07	----	----	----	----	----
DBC	0.34	----	0.63± 0.16	1.27± 0.32	----	----	0.77± 0.14	0.69± 0.14	----	----	0.37± 0.05	0.46± 0.12	----	----	----	----	----
L23BC	----	0.48± 0.18	0.50± 0.07	0.84± 0.10	0.18± 0.03	----	0.72± 0.15	0.68± 0.05	----	1.60± 0.23	0.39± 0.05	0.42± 0.17	0.51± 0.11	----	----	----	1.08± 0.30
ChC	0.47± 0.16	----	0.52± 0.11	0.90± 0.19	----	----	----	0.69± 0.26	0.47± 0.15	----	0.54± 0.25	0.53± 0.16	----	----	----	----	----
L23Pyr	----	0.53± 0.07	0.31± 0.05	0.71± 0.11	0.28± 0.11	----	0.52± 0.12	0.48± 0.05	0.35± 0.03	0.34± 0.08	0.25± 0.05	0.56± 0.19	0.35± 0.16	----	----	----	----
L5MC	----	----	----	0.55± 0.16	----	0.30± 0.07	----	0.65	----	0.53± 0.12	----	0.86± 0.29	0.41± 0.11	----	----	0.30± 0.02	0.52± 0.09
L5NGC	----	----	0.37	0.68± 0.20	----	----	----	----	----	----	0.36± 0.21	1.36± 0.83	0.17± 0.03	0.28	----	----	----
L5BC	----	----	0.23± 0.00	0.62± 0.17	----	0.21	----	0.79± 0.18	----	1.32± 0.20	0.40± 0.08	0.99± 0.32	1.19± 0.18	0.53	----	----	1.20± 0.12
SC	----	----	----	0.52± 0.15	----	----	----	0.25	----	----	0.48± 0.08	0.98± 0.22	0.60± 0.17	1.40± 0.34	----	----	----
HEC	----	----	----	0.35± 0.04	----	----	----	0.56± 0.16	----	1.15± 0.28	0.45± 0.08	1.59± 0.77	0.43	----	0.81±0.26	----	0.53± 0.07
DC	----	----	----	0.68± 0.16	----	----	----	----	----	----	0.33± 0.07	1.01± 0.27	----	----	----	----	----
L5Pyr	----	0.42± 0.07	0.22± 0.06	0.45± 0.08	----	----	0.15± 0.03	0.20± 0.02	----	1.13± 0.35	0.27± 0.03	0.90± 0.22	0.81± 0.16	0.44± 0.04	0.90± 0.20	----	----

Table S6. Amplitude of uIPSPs and uEPSPs.

Table S7. Connectivity among PV^+ neurons and pyramidal neurons

postsynaptic \ presynaptic	L23 BC	ChC	L23Pyr	L5BC	SC	HEC	L5Pyr
L23 BC	41.2% (28/68)	0% (0/5)	15.9% (13/82)	19.3% (6/31)	0% (0/15)	0% (0/12)	0% (0/56)
ChC	0% (0/5)	---	0% (0/1)	----	0% (0/1)	----	0% (0/1)
L23Pyr	32.9% (27/82)	0% (0/1)	2% (1/50)	0% (0/15)	0% (0/10)	0% (0/12)	0% (0/50)
L5BC	12.9% (4/31)	---	13.3% (2/15)	42.8% (3/7)	0% (0/6)	0% (0/5)	15% (3/20)
SC	0% (0/15)	0% (0/1)	0% (0/10)	0% (0/6)	50.0% (3/6)	0% (0/3)	0% (0/10)
HEC	0% (0/12)	---	8.3% (1/12)	0% (0/5)	0% (0/3)	42.8% (3/7)	0% (0/6)
L5Pyr	7.1% (4/56)	0% (0/1)	5.1% (2/39)	25% (5/20)	16.7% (1/6)	33.4% (2/6)	0% (0/12)

Table S7. Connectivity among distinct types of PV^+ neurons and their interconnections with pyramidal neurons. Note that the connectivity pattern showed by the above matrix is similar to that described in Fig.4, and Fig.S14.

Table S8. Connectivity among SOM$^+$ neurons and pyramidal neurons							
postsynaptic \ presynaptic	L23 MC	L23 BTC	L23 BC	L23 Pyr	L5MC	L5 BC	L5 Pyr
L23 MC	0% (0/63)	40% (4/10)	11.1% (1/9)	20.4% (10/49)	0% (0/56)	0% (0/31)	0% (0/31)
L23 BTC	40% (4/10)	0% (0/2)	0% (0/2)	22.2% (2/9)	0% (0/5)	0% (0/2)	0% (0/6)
L23 BC	33.3% (3/9)	0% (0/2)	25% (1/4)	10.5% (2/19)	8.3% (1/12)	11.1% (1/9)	0% (0/10)
L23 Pyr	38.8% (19/49)	33.3% (4/12)	21.1% (4/19)	0% (0/25)	15.9% (7/44)	20% (3/15)	0% (0/33)
L5 MC	0% (0/56)	0% (0/5)	0% (0/12)	13.6% (6/44)	0% (0/26)	0% (0/6)	6.7% (2/30)
L5 BC	0% (0/31)	0% (0/2)	0% (0/9)	0% (0/15)	0% (0/6)	25.0% (3/12)	5.6% (1/18)
L5 Pyr	3.2% (1/31)	0% (0/6)	0% (0/10)	3.0% (1/33)	12.8% (4/30)	16.7% (3/18)	0% (0/16)

Table S8. Connectivity among distinct types of SOM$^+$ neurons and their interconnections with pyramidal neurons. Note that the connectivity pattern showed by the above matrix is generally similar to that described in Fig.4, and Fig.S14.

Table S9. Connectivity among VIP$^+$ neurons and pyramidal neurons				
postsynaptic \ presynaptic	BTC	BPC	L23Pyr	L5Pyr
BTC	7.7% (2/26)	0% (0/32)	21% (4/19)	0% (0/18)
BPC	6.7% (2/32)	0% (0/22)	0% (0/19)	0% (0/17)
L23Pyr	10.5% (2/19)	0% (0/18)	0% (0/20)	0% (0/20)
L5Pyr	0% (0/18)	0% (0/17)	5% (1/20)	0% (0/10)

Table S9. Connectivity among distinct types of VIP$^+$ neurons and their interconnections with pyramidal neurons. Note that the connectivity pattern showed by the above matrix is generally similar to that described in Fig.4, and Fig.S14.

Table S10. Connectivity of L5P-ST and L5P-TT with Interneurons

presynaptic \ postsynaptic	L5P-TT	L5P-ST	*P*
SBC-like	0.0% (0/28)	0.0% (0/49)	--
eNGC	11.1% (2/18)	10.8% (4/37)	0.97
L23MC	8.3% (2/24)	8.0% (4/50)	0.96
L23NGC	38.1% (8/21)	32.1% (18/56)	0.62
BTC	0.0% (0/26)	0.0% (0/53)	--
BPC	0.0% (0/20)	0.0% (0/48)	--
DBC	9.5% (2/11)	11.6% (3/26)	0.59
L23BC	6.7% (4/60)	5.6% (7/125)	0.77
ChC	0.0% (0/5)	0.0% (0/9)	--
L23P	3.9% (2/51)	4.1% (4/98)	0.96
L5MC	23.3% (7/30)	20.0% (16/80)	0.70
L5NGC	66.7% (2/3)	62.5% (5/8)	0.90
L5BC	31.0% (9/29)	23.3% (24/103)	0.40
SC	7.1% (1/14)	10.0% (3/30)	0.76
HEC	42.8% (6/14)	27.7% (10/36)	0.30
L5P-TT	0.0% (0/12)	0.0% (0/36)	--
L5P-ST	0.0% (0/36)	0.0% (0/66)	--

postsynaptic \ presynaptic	L5P-TT	L5P-ST	*P*
SBC-like	0.0% (0/24)	0.0% (0/41)	--
eNGC	0.0% (0/19)	2.4% (1/41)	0.49
L23MC	0.0% (0/24)	0.0% (0/50)	--
L23NGC	0.0% (0/20)	3.7% (2/54)	0.39
BTC	0.0% (0/23)	0.0% 0/50	--
BPC	0.0% (0/19)	0.0% (0/46)	--
DBC	0.0% (0/10)	0.0% (0/24)	--
L23BC	1.8% (1/55)	3.8% 4/118	0.57
ChC	0.0% (0/5)	0.0% (0/9)	--
L23P	0.0% (0/51)	0.0% (0/98)	--
L5MC	10.0% (3/30)	7.1% (5/70)	0.63
L5NGC	0.0% (0/3)	0.0% (0/9)	--
L5BC	9.5% (2/21)	11.7% (11/94)	0.78
SC	0.0% (0/12)	0.0% (0/29)	--
HEC	21.4% (3/14)	15.6% (5/32)	0.63

Table S10. Connectivity of thick-tufted L5 pyramidal neurons and (L5P-TT) and slender-tufted L5 pyramidal neurons (L5P-ST) with interneurons. The probability of finding a connected pair of neurons between two specific types of neurons is denoted as % (total connections found/total connections tested). There is no significant difference between two types of L5 pyramidal neurons in connecting with interneurons ($p > 0.05$).

References

1. H. Markram, M. Toledo-Rodriguez, Y. Wang, A. Gupta, G. Silberberg, C. Wu, Interneurons of the neocortical inhibitory system. *Nat. Rev. Neurosci.* **5**, 793–807 (2004). Medline doi:10.1038/nrn1519

2. J. DeFelipe, P. L. López-Cruz, R. Benavides-Piccione, C. Bielza, P. Larrañaga, S. Anderson, A. Burkhalter, B. Cauli, A. Fairén, D. Feldmeyer, G. Fishell, D. Fitzpatrick, T. F. Freund, G. González-Burgos, S. Hestrin, S. Hill, P. R. Hof, J. Huang, E. G. Jones, Y. Kawaguchi, Z. Kisvárday, Y. Kubota, D. A. Lewis, O. Marín, H. Markram, C. J. McBain, H. S. Meyer, H. Monyer, S. B. Nelson, K. Rockland, J. Rossier, J. L. Rubenstein, B. Rudy, M. Scanziani, G. M. Shepherd, C. C. Sherwood, J. F. Staiger, G. Tamás, A. Thomson, Y. Wang, R. Yuste, G. A. Ascoli, New insights into the classification and nomenclature of cortical GABAergic interneurons. *Nat. Rev. Neurosci.* **14**, 202–216 (2013). Medline

3. D. Dumitriu, R. Cossart, J. Huang, R. Yuste, Correlation between axonal morphologies and synaptic input kinetics of interneurons from mouse visual cortex. *Cereb. Cortex* **17**, 81–91 (2007). Medline doi:10.1093/cercor/bhj126

4. G. A. Ascoli, L. Alonso-Nanclares, S. A. Anderson, G. Barrionuevo, R. Benavides-Piccione, A. Burkhalter, G. Buzsáki, B. Cauli, J. Defelipe, A. Fairén, D. Feldmeyer, G. Fishell, Y. Fregnac, T. F. Freund, D. Gardner, E. P. Gardner, J. H. Goldberg, M. Helmstaedter, S. Hestrin, F. Karube, Z. F. Kisvárday, B. Lambolez, D. A. Lewis, O. Marin, H. Markram, A. Muñoz, A. Packer, C. C. Petersen, K. S. Rockland, J. Rossier, B. Rudy, P. Somogyi, J. F. Staiger, G. Tamas, A. M. Thomson, M. Toledo-Rodriguez, Y. Wang, D. C. West, R. Yuste; Petilla Interneuron Nomenclature Group, Petilla terminology: Nomenclature of features of GABAergic interneurons of the cerebral cortex. *Nat. Rev. Neurosci.* **9**, 557–568 (2008). Medline doi:10.1038/nrn2402

5. X. Jiang, G. Wang, A. J. Lee, R. L. Stornetta, J. J. Zhu, The organization of two new cortical interneuronal circuits. *Nat. Neurosci.* **16**, 210–218 (2013). Medline doi:10.1038/nn.3305

6. A. Kepecs, G. Fishell, Interneuron cell types are fit to function. *Nature* **505**, 318–326 (2014). Medline doi:10.1038/nature12983

7. C. Le Magueresse, H. Monyer, GABAergic interneurons shape the functional maturation of the cortex. *Neuron* **77**, 388–405 (2013). Medline doi:10.1016/j.neuron.2013.01.011

8. Z. J. Huang, G. Di Cristo, F. Ango, Development of GABA innervation in the cerebral and cerebellar cortices. *Nat. Rev. Neurosci.* **8**, 673–686 (2007). Medline doi:10.1038/nrn2188

9. J. Ting, T. Daigle, Q. Chen, G. Feng, in *Patch-Clamp Methods and Protocols*, M. Martina, S. Taverna, Eds. (Springer New York, 2014), vol. 1183, chap. 14, pp. 221-242.

10. H. S. Meyer, D. Schwarz, V. C. Wimmer, A. C. Schmitt, J. N. Kerr, B. Sakmann, M. Helmstaedter, Inhibitory interneurons in a cortical column form hot zones of inhibition in layers 2 and 5A. *Proc. Natl. Acad. Sci. U.S.A.* **108**, 16807–16812 (2011). Medline doi:10.1073/pnas.1113648108

11. G. S. Jefferis, C. J. Potter, A. M. Chan, E. C. Marin, T. Rohlfing, C. R. Maurer Jr., L. Luo, Comprehensive maps of *Drosophila* higher olfactory centers: Spatially segregated fruit and pheromone representation. *Cell* **128**, 1187–1203 (2007). Medline doi:10.1016/j.cell.2007.01.040

12. S. Hestrin, W. E. Armstrong, Morphology and physiology of cortical neurons in layer I. *J. Neurosci.* **16**, 5290–5300 (1996). Medline

13. Y. Wang, M. Toledo-Rodriguez, A. Gupta, C. Wu, G. Silberberg, J. Luo, H. Markram, Anatomical, physiological and molecular properties of Martinotti cells in the somatosensory cortex of the juvenile rat. *J. Physiol.* **561**, 65–90 (2004). Medline doi:10.1113/jphysiol.2004.073353

14. A. Gupta, Y. Wang, H. Markram, Organizing principles for a diversity of GABAergic interneurons and synapses in the neocortex. *Science* **287**, 273–278 (2000). Medline doi:10.1126/science.287.5451.273

15. K. A. Buchanan, A. V. Blackman, A. W. Moreau, D. Elgar, R. P. Costa, T. Lalanne, A. A. Tudor Jones, J. Oyrer, P. J. Sjöström, Target-specific expression of presynaptic NMDA receptors in neocortical microcircuits. *Neuron* **75**, 451–466 (2012). Medline doi:10.1016/j.neuron.2012.06.017

16. M. Le Bon-Jego, R. Yuste, Persistently active, pacemaker-like neurons in neocortex. *Front. Neurosci.* **1**, 123–129 (2007). Medline doi:10.3389/neuro.01.1.1.009.2007

17. Z. Xiang, D. A. Prince, Heterogeneous actions of serotonin on interneurons in rat visual cortex. *J. Neurophysiol.* **89**, 1278–1287 (2003). Medline doi:10.1152/jn.00533.2002

18. H.-T. Chao, H. Chen, R. C. Samaco, M. Xue, M. Chahrour, J. Yoo, J. L. Neul, S. Gong, H. C. Lu, N. Heintz, M. Ekker, J. L. Rubenstein, J. L. Noebels, C. Rosenmund, H. Y. Zoghbi, Dysfunction in GABA signalling mediates autism-like stereotypies and Rett syndrome phenotypes. *Nature* **468**, 263–269 (2010). Medline doi:10.1038/nature09582

19. H. Hu, J. Z. Cavendish, A. Agmon, Not all that glitters is gold: Off-target recombination in the somatostatin-IRES-Cre mouse line labels a subset of fast-spiking interneurons. *Front. Neural Circuits* **7**, 195 (2013). Medline doi:10.3389/fncir.2013.00195

20. M. Nassar, J. Simonnet, R. Lofredi, I. Cohen, E. Savary, Y. Yanagawa, R. Miles, D. Fricker, Diversity and overlap of parvalbumin and somatostatin expressing interneurons in mouse presubiculum. *Front. Neural Circuits* **9**, 20 (2015). Medline doi:10.3389/fncir.2015.00020

21. J. T. Porter, B. Cauli, J. F. Staiger, B. Lambolez, J. Rossier, E. Audinat, Properties of bipolar VIPergic interneurons and their excitation by pyramidal neurons in the rat neocortex. *Eur. J. Neurosci.* **10**, 3617–3628 (1998). Medline doi:10.1046/j.1460-9568.1998.00367.x

22. B. Cauli, E. Audinat, B. Lambolez, M. C. Angulo, N. Ropert, K. Tsuzuki, S. Hestrin, J. Rossier, Molecular and physiological diversity of cortical nonpyramidal cells. *J. Neurosci.* **17**, 3894–3906 (1997). Medline

23. Y. Kawaguchi, Y. Kubota, Physiological and morphological identification of somatostatin- or vasoactive intestinal polypeptide-containing cells among GABAergic cell subtypes in rat frontal cortex. *J. Neurosci.* **16**, 2701–2715 (1996). Medline

24. S. Lee, J. Hjerling-Leffler, E. Zagha, G. Fishell, B. Rudy, The largest group of superficial neocortical GABAergic interneurons expresses ionotropic serotonin receptors. *J. Neurosci.* **30**, 16796–16808 (2010). Medline doi:10.1523/JNEUROSCI.1869-10.2010

25. G. Tamás, A. Lorincz, A. Simon, J. Szabadics, Identified sources and targets of slow inhibition in the neocortex. *Science* **299**, 1902–1905 (2003). Medline doi:10.1126/science.1082053

26. S. Oláh, M. Füle, G. Komlósi, C. Varga, R. Báldi, P. Barzó, G. Tamás, Regulation of cortical microcircuits by unitary GABA-mediated volume transmission. *Nature* **461**, 1278–1281 (2009). Medline doi:10.1038/nature08503

27. R. Chittajallu, K. A. Pelkey, C. J. McBain, Neurogliaform cells dynamically regulate somatosensory integration via synapse-specific modulation. *Nat. Neurosci.* **16**, 13–15 (2013). Medline doi:10.1038/nn.3284

28. C. K. Pfeffer, M. Xue, M. He, Z. J. Huang, M. Scanziani, Inhibition of inhibition in visual cortex: The logic of connections between molecularly distinct interneurons. *Nat. Neurosci.* **16**, 1068–1076 (2013). Medline doi:10.1038/nn.3446

29. S. Lee, I. Kruglikov, Z. J. Huang, G. Fishell, B. Rudy, A disinhibitory circuit mediates motor integration in the somatosensory cortex. *Nat. Neurosci.* **16**, 1662–1670 (2013). Medline doi:10.1038/nn.3544

30. H. J. Pi, B. Hangya, D. Kvitsiani, J. I. Sanders, Z. J. Huang, A. Kepecs, Cortical interneurons that specialize in disinhibitory control. *Nature* **503**, 521–524 (2013). Medline doi:10.1038/nature12676

31. H. Taniguchi, M. He, P. Wu, S. Kim, R. Paik, K. Sugino, D. Kvitsiani, Y. Fu, J. Lu, Y. Lin, G. Miyoshi, Y. Shima, G. Fishell, S. B. Nelson, Z. J. Huang, A resource of Cre driver lines for genetic targeting of GABAergic neurons in cerebral cortex. *Neuron* **71**, 995–1013 (2011). Medline doi:10.1016/j.neuron.2011.07.026

32. J. Reimer, E. Froudarakis, C. R. Cadwell, D. Yatsenko, G. H. Denfield, A. S. Tolias, Pupil fluctuations track fast switching of cortical states during quiet wakefulness. *Neuron* **84**, 355–362 (2014). Medline doi:10.1016/j.neuron.2014.09.033

33. C. Wozny, S. R. Williams, Specificity of synaptic connectivity between layer 1 inhibitory interneurons and layer 2/3 pyramidal neurons in the rat neocortex. *Cereb. Cortex* **21**, 1818–1826 (2011). Medline doi:10.1093/cercor/bhq257

34. N. V. De Marco García, R. Priya, S. N. Tuncdemir, G. Fishell, T. Karayannis, Sensory inputs control the integration of neurogliaform interneurons into cortical circuits. *Nat. Neurosci.* **18**, 393–401 (2015). Medline doi:10.1038/nn.3946

35. X. Xu, E. M. Callaway, Laminar specificity of functional input to distinct types of inhibitory cortical neurons. *J. Neurosci.* **29**, 70–85 (2009). Medline doi:10.1523/JNEUROSCI.4104-08.2009

36. H. Markram, J. Lübke, M. Frotscher, A. Roth, B. Sakmann, Physiology and anatomy of synaptic connections between thick tufted pyramidal neurones in the developing rat neocortex. *J. Physiol.* **500**, 409–440 (1997). Medline doi:10.1113/jphysiol.1997.sp022031

37. R. Perin, T. K. Berger, H. Markram, A synaptic organizing principle for cortical neuronal groups. *Proc. Natl. Acad. Sci. U.S.A.* **108**, 5419–5424 (2011). Medline doi:10.1073/pnas.1016051108

38. D. R. Dajani, L. Q. Uddin, Local brain connectivity across development in autism spectrum disorder: A cross-sectional investigation. *Autism Res.* **xxx**, xxx (2015). Medline

39. K. Menuz, R. A. Nicoll, Loss of inhibitory neuron AMPA receptors contributes to ataxia and epilepsy in stargazer mice. *J. Neurosci.* **28**, 10599–10603 (2008). Medline doi:10.1523/JNEUROSCI.2732-08.2008

40. F. A. Chaudhry, R. J. Reimer, E. E. Bellocchio, N. C. Danbolt, K. K. Osen, R. H. Edwards, J. Storm-Mathisen, The vesicular GABA transporter, VGAT, localizes to synaptic vesicles in sets of glycinergic as well as GABAergic neurons. *J. Neurosci.* **18**, 9733–9750 (1998). Medline

41. S. M. Wojcik, S. Katsurabayashi, I. Guillemin, E. Friauf, C. Rosenmund, N. Brose, J. S. Rhee, A shared vesicular carrier allows synaptic corelease of GABA and glycine. *Neuron* **50**, 575–587 (2006). Medline doi:10.1016/j.neuron.2006.04.016

42. A. J. Lee, G. Wang, X. Jiang, S. M. Johnson, E. T. Hoang, F. Lanté, R. L. Stornetta, M. P. Beenhakker, Y. Shen, J. Julius Zhu, Canonical organization of layer 1 neuron-led cortical inhibitory and disinhibitory interneuronal circuits. *Cereb. Cortex* (2014). Medline

43. J. T. F. Ting, paper presented at the Society for Neuroscience 2011 annual meeting, Washington, DC, 14 November 2011.

44. S. Lefort, C. Tomm, J. C. Floyd Sarria, C. C. Petersen, The excitatory neuronal network of the C2 barrel column in mouse primary somatosensory cortex. *Neuron* **61**, 301–316 (2009). Medline doi:10.1016/j.neuron.2008.12.020

45. G. Qi, G. Radnikow, D. Feldmeyer, Electrophysiological and morphological characterization of neuronal microcircuits in acute brain slices using paired patch-clamp recordings. *J. Vis. Exp.* **95**, 52358 (2015). Medline

46. H. Cuntz, F. Forstner, A. Borst, M. Häusser, The TREES toolbox—probing the basis of axonal and dendritic branching. *Neuroinformatics* **9**, 91–96 (2011). Medline doi:10.1007/s12021-010-9093-7

47. H. Cuntz, F. Forstner, A. Borst, M. Häusser, One rule to grow them all: A general theory of neuronal branching and its practical application. *PLOS Comput. Biol.* **6**, e1000877 (2010). Medline doi:10.1371/journal.pcbi.1000877

48. G. M. Shepherd, A. Stepanyants, I. Bureau, D. Chklovskii, K. Svoboda, Geometric and functional organization of cortical circuits. *Nat. Neurosci.* **8**, 782–790 (2005). Medline doi:10.1038/nn1447

49. J. Friedman, T. Hastie, R. Tibshirani, Regularization paths for generalized linear models via coordinate descent. *J. Stat. Softw.* **33**, 1–22 (2010). Medline doi:10.18637/jss.v033.i01

50. J. D. Hunter, Matplotlib: A 2D graphics environment. *Comput. Sci. Eng.* **9**, 90–95 (2007). doi:10.1109/MCSE.2007.55

51. Y. Ma, H. Hu, A. S. Berrebi, P. H. Mathers, A. Agmon, Distinct subtypes of somatostatin-containing neocortical interneurons revealed in transgenic mice. *J. Neurosci.* **26**, 5069–5082 (2006). Medline doi:10.1523/JNEUROSCI.0661-06.2006

52. Y. Kawaguchi, Physiological subgroups of nonpyramidal cells with specific morphological characteristics in layer II/III of rat frontal cortex. *J. Neurosci.* **15**, 2638–2655 (1995). Medline

53. S. Oláh, G. Komlósi, J. Szabadics, C. Varga, E. Tóth, P. Barzó, G. Tamás, Output of neurogliaform cells to various neuron types in the human and rat cerebral cortex. *Front. Neural Circuits* **1**, 4 (2007). Medline doi:10.3389/neuro.04.004.2007

54. M. Galarreta, S. Hestrin, Electrical and chemical synapses among parvalbumin fast-spiking GABAergic interneurons in adult mouse neocortex. *Proc. Natl. Acad. Sci. U.S.A.* **99**, 12438–12443 (2002). Medline doi:10.1073/pnas.192159599

55. B. Cauli, J. T. Porter, K. Tsuzuki, B. Lambolez, J. Rossier, B. Quenet, E. Audinat, Classification of fusiform neocortical interneurons based on unsupervised clustering. *Proc. Natl. Acad. Sci. U.S.A.* **97**, 6144–6149 (2000). Medline doi:10.1073/pnas.97.11.6144

56. C. Allene, J. Lourenço, A. Bacci, The neuronal identity bias behind neocortical GABAergic plasticity. *Trends Neurosci.* **38**, 524–534 (2015). Medline doi:10.1016/j.tins.2015.07.008

57. Á. L. Bodor, I. Katona, G. Nyíri, K. Mackie, C. Ledent, N. Hájos, T. F. Freund, Endocannabinoid signaling in rat somatosensory cortex: Laminar differences and involvement of specific interneuron types. *J. Neurosci.* **25**, 6845–6856 (2005). Medline doi:10.1523/JNEUROSCI.0442-05.2005

58. Y. Kawaguchi, S. Kondo, Parvalbumin, somatostatin and cholecystokinin as chemical markers for specific GABAergic interneuron types in the rat frontal cortex. *J. Neurocytol.* **31**, 277–287 (2002). Medline doi:10.1023/A:1024126110356

59. P. R. Hof, I. I. Glezer, F. Condé, R. A. Flagg, M. B. Rubin, E. A. Nimchinsky, D. M. Vogt Weisenhorn, Cellular distribution of the calcium-binding proteins parvalbumin, calbindin, and calretinin in the neocortex of mammals: Phylogenetic and developmental patterns. *J. Chem. Neuroanat.* **16**, 77–116 (1999). Medline doi:10.1016/S0891-0618(98)00065-9

60. Y. Gonchar, Q. Wang, A. H. Burkhalter, Multiple distinct subtypes of GABAergic neurons in mouse visual cortex identified by triple immunostaining. *Front. Neuroanat.* **1**, 3 (2008). Medline

61. H. Ko, L. Cossell, C. Baragli, J. Antolik, C. Clopath, S. B. Hofer, T. D. Mrsic-Flogel, The emergence of functional microcircuits in visual cortex. *Nature* **496**, 96–100 (2013). Medline doi:10.1038/nature12015

62. C. Q. Chiu, G. Lur, T. M. Morse, N. T. Carnevale, G. C. Ellis-Davies, M. J. Higley, Compartmentalization of GABAergic inhibition by dendritic spines. *Science* **340**, 759–762 (2013). Medline doi:10.1126/science.1234274

63. S. R. Williams, S. J. Mitchell, Direct measurement of somatic voltage clamp errors in central neurons. *Nat. Neurosci.* **11**, 790–798 (2008). Medline doi:10.1038/nn.2137

64. K. D. Harris, G. M. G. Shepherd, The neocortical circuit: Themes and variations. *Nat. Neurosci.* **18**, 170–181 (2015). Medline doi:10.1038/nn.3917